



THE UNIVERSITY *of* EDINBURGH

## Edinburgh Research Explorer

### **Intrinsic conditions of magma genesis at the Lunar Crater Volcanic Field (Nevada), and implications for internal plumbing and magma ascent**

**Citation for published version:**

Cortes, JA, Smith, E, Valentine, G, Johnsen, R, Rasoazanamparany, C, Widom, E, Sas, M & Ruth, D 2015, 'Intrinsic conditions of magma genesis at the Lunar Crater Volcanic Field (Nevada), and implications for internal plumbing and magma ascent', *American Mineralogist*, vol. 100, pp. 396. <https://doi.org/10.2138/am-2015-4812>

**Digital Object Identifier (DOI):**

[10.2138/am-2015-4812](https://doi.org/10.2138/am-2015-4812)

**Link:**

[Link to publication record in Edinburgh Research Explorer](#)

**Published In:**

American Mineralogist

**General rights**

Copyright for the publications made accessible via the Edinburgh Research Explorer is retained by the author(s) and / or other copyright owners and it is a condition of accessing these publications that users recognise and abide by the legal requirements associated with these rights.

**Take down policy**

The University of Edinburgh has made every reasonable effort to ensure that Edinburgh Research Explorer content complies with UK legislation. If you believe that the public display of this file breaches copyright please contact [openaccess@ed.ac.uk](mailto:openaccess@ed.ac.uk) providing details, and we will remove access to the work immediately and investigate your claim.



# Revision 3

## **INTRINSIC CONDITIONS OF MAGMAS FROM THE LUNAR CRATER VOLCANIC FIELD (NEVADA): IMPLICATIONS FOR INTERNAL PLUMBING AND MAGMA ASCENT.**

Joaquín A. Cortés<sup>1,2\*</sup>, Eugene I. Smith<sup>3</sup>, Greg A. Valentine<sup>1</sup>, Racheal Johnsen<sup>3</sup>, Christine Rasoazanamparany<sup>4</sup>, Elisabeth Widom<sup>4</sup>, Mai Sas<sup>3,5</sup>, Dawn Ruth<sup>1</sup>.

<sup>1</sup> Department of Geology, 411 Cooke Hall, Buffalo, NY 14260, University at Buffalo, State University of New York, USA.

<sup>2</sup> School of GeoSciences, The University of Edinburgh, Grant Institute, The King's Buildings, West Mains Road, Edinburgh EH9 3JW, UK.

<sup>3</sup> Department of Geoscience, 4505 S. Maryland Parkway, Las Vegas, NV 89154, University of Nevada Las Vegas, USA.

<sup>4</sup> Department of Geology, 114 Shideler Hall, Oxford, OH 45056, Miami University, USA.

<sup>5</sup> Department of Geology, 516 High Street, Bellingham, WA 98225-9080, Western Washington University, USA.

\*Corresponding Author, [caco@buffalo.edu](mailto:caco@buffalo.edu)

American Mineralogist, special issue “Volcanic Rocks”

## ABSTRACT

The northern part of the Lunar Crater Volcanic Field (central Nevada, USA) contains more than one hundred Quaternary basaltic cones and maars and related eruptive products. We focused on four informal units of different ages and locations in the field to test the compositional variability and magma ascent processes within the time span of an individual eruption and the variability between very closely spaced volcanoes with different ages. Based in whole-rock chemistry, mineral chemistry and the calculation of intrinsic properties (pressure, temperature and oxygen fugacity) we found that individual magma batches were generated in the asthenospheric mantle from a heterogeneous garnet lherzolite/olivine websterite source by ~3-5% partial melting. Each magma batch and temporary deep reservoir was a separate entity rather than part of a continuous long-lived reservoir. Magmas ascended relatively fast, stalled and crystallized in the uppermost several kilometres of the mantle near the base of the crust and also stalled at mid-crustal levels with minor or no geochemical interaction with surrounding rocks. Our data also suggest that volcanoes erupting within certain time windows have similar source characteristics and ascent processes whether they are located within a few hundred meters of each other or are separated by many kilometres.

Keywords: Lunar Crater Volcanic Field, monogenetic volcanism, whole-rock chemistry, mineral chemistry, geothermobarometry.

## INTRODUCTION

Most of Earth's volcanism occurs at plate boundaries, in association with rifting or subduction, or in high magma-flux intraplate hotspots. However, substantial volcanism also occurs within continents and ocean basins, forming intraplate volcanic fields with relatively low magma fluxes and

69 commonly consisting of small-volume mafic volcanoes with alkaline affinities. Continental intraplate  
70 volcanic fields can consist of one to several hundred individual volcanoes, most of which are  
71 monogenetic (erupt in a single episode lasting weeks to years), and have lifespans of a few million  
72 years (Connor and Conway, 2000). Unlike “hotspot” systems, these fields tend to have a diffuse  
73 spatial distribution of eruptive centers and in many cases have no clear migration of eruptive activity  
74 with time. Volcanic landforms in intraplate fields are dominated by scoria cones, spatter/agglomerate  
75 ramparts, lava fields, maars, and tuff cones, in proportions that depend upon the relative dominance of  
76 explosive versus effusive activity and the local hydrologic environment (Valentine and Gregg, 2008;  
77 White and Ross, 2011; Brown and Valentine, 2013).

78 Petrologic studies of intraplate volcanism have tended to focus on “big picture” questions such  
79 as the nature of the mantle, or the broad evolution of regional magmatic activity over millions of years;  
80 however, recent studies have begun to explore the details of volcanic fields with much higher spatial  
81 and temporal resolution, including the complexities often recorded within individual monogenetic  
82 volcanoes. An advantage of a study of low magma-volume monogenetic volcanoes is that they may  
83 display compositional complexities that are closely related to mantle source characteristics, which may  
84 be totally overprinted by crustal reservoir processes in higher volume-flux, long-lived volcanoes.  
85 Geochemical and volcanological data from the Plio-Pleistocene Southwest Nevada Volcanic Field in  
86 the western U.S.A. for example, suggest that individual volcanoes tap domains of partial melt that are  
87 progressively decreasing in volume and degree of partial melting with time (Valentine and Perry,  
88 2007). The domains are inferred to reflect local enrichments in volatile components within the  
89 lithospheric mantle source that has been subjected to repeated metasomatic events over ~1 Ga.  
90 Valentine and Perry (2006, 2007) suggested that the length scales of the partial melt domains are on the  
91 order of kilometers in size and the size of each volcano is proportional to its melt domain size. Brenna  
92 et al. (2012) showed how the Jeju Volcanic Field (South Korea) records deepening, increasing degree  
93 of melting, and increased melt volumes through time. Detailed studies of individual volcanoes within

94 the Jeju field indicate that each eruption tapped a domain of partial melt on the order of a few  
95 kilometers in size and each with a slightly unique composition that may vary within individual  
96 eruptions, reflecting mantle heterogeneity (Brenna et al., 2010). The Auckland Volcanic Field (New  
97 Zealand) shows similar behavior, with the volumes of individual volcanoes being correlated positively  
98 with the degree and spatial scale of partial melting in the asthenospheric source, but with large-volume  
99 melt batches interacting more extensively with lithospheric melts compared to smaller batches (McGee  
100 et al., 2013). Within the Auckland field, detailed data from the Motukorea volcanic center illustrates  
101 complex magma source history even within an individual monogenetic eruption that would commonly  
102 be assumed to be a “single batch.” Other detailed studies support the perspective that despite their  
103 relatively small volumes (typically less than  $\sim 1 \text{ km}^3$ ) and short lives; monogenetic volcanoes are  
104 accompanied by relatively complex processes related to magma sources, ascent, and temporary storage  
105 (e.g; Parícutín: Rowe et al., 2011; Erlund et al., 2009; Pioli et al., 2008; Luhr and Simkin, 1993;  
106 Jorullo: Johnson et al., 2008). Questions remain, however, as to whether the temporal and spatial  
107 scales of mantle source domains and the subsequent ascent and eruption of magmas have consistent  
108 relationships within and between volcanic fields.

109 In this work we focus on the products of four monogenetic volcanoes in the Lunar Crater  
110 Volcanic Field (central Nevada, USA) to explore two questions. (1) What are the compositional  
111 variability and magma ascent processes within the time span of an individual eruption? (2) What is the  
112 variability between very closely spaced volcanoes with different ages? Trace element data presented  
113 here suggest some degree of small-scale heterogeneity in the asthenospheric mantle, consistent with  
114 isotopic data (Rasoazanamparany et al., in review). Thermodynamic calculations of intrinsic variables  
115 show that parent melts ascended through two types of magma feeding systems: one in which magma  
116 ponded at or just below the base of the crust, and a second where magmas also ponded at mid-crustal  
117 levels. The volcanoes were fed by small magma batches that had essentially no chemical interaction  
118 with the crust, and ascended rapidly between storage levels and to the surface. In the cases studied,

119 two early eruptions tapped slightly variable mantle source rocks, and the two younger eruptions tapped  
120 a different source but one that was relatively homogeneous in space over a length scale of several  
121 kilometres and across a time span of several tens of thousands of years. Differences in composition  
122 and feeding systems between individual volcanoes seems to be more sensitive to time windows than to  
123 spatial variability in the source or crustal plumbing systems.

124

## 125 **GEOLOGICAL SETTING AND PREVIOUS WORK**

126

127 The Lunar Crater Volcanic Field (LCVF) lies at the northern end of a belt of scattered, Plio-  
128 Pleistocene basaltic fields that extends north-northeast from Death Valley (California) into central  
129 Nevada (Vaniman et al., 1982). The field is in the Basin and Range Province, a broad area of  
130 extensional tectonics, but is located centrally within the Province while most other young volcanic  
131 fields are found around its edge (e.g., Smith and Leudke, 1984; Brown et al. 2010; Gazel et al., 2012).  
132 The LCVF contains more than 100 individual cones with attendant lava fields, and four maars  
133 (Valentine et al., 2011; Hintz and Valentine, 2012; Valentine and Cortés, 2013), covering an area of 80  
134 by 20 km extending from the Reveille Range to the Pancake Range (Figure 1).

135 Previous work in the LCVF has focused on geochemical and petrologic evolution of the field as  
136 a whole or of major parts of it, differently from our focus on more local scales (Scott, 1969; Scott and  
137 Trask, 1971; Bergman et al., 1981; Bergman, 1982; Lum, 1986; Kargel, 1986); see summary by Foland  
138 and Bergman (1992). Several authors used isotopic compositions of LCVF rocks along with samples  
139 from many volcanic fields in the western U.S.A. to define regional mantle isotopic domains (Lum et  
140 al., 1989; Menzies, 1989; Farmer et al., 1989). In general, isotopic, trace element, and xenolith  
141 geothermometry data (Smith, 2000) suggest that the LCVF magmas are sourced in the asthenosphere  
142 with characteristics of ocean island basalt (OIB) (Foland and Bergman, 1992), and with evidence of  
143 early contamination by crustal rocks (mainly carbonates beneath the early Pliocene Reveille Range

144 volcanoes; Yogodzinski et al., 1996) and by lithospheric mantle (potentially veinlets of intermediate  
145 composition in the younger Pancake Range volcanoes; Dickson, 1997).

146

## 147 **FIELD DESCRIPTION, STRATIGRAPHY AND PETROGRAPHY**

148

149 We focus on four different basaltic eruptive units (red area in Figures 1, 2), which are here  
150 informally named (from youngest to oldest): Marcath (a.k.a. Black Rock, with cosmogenic exposure  
151 age of  $38 \pm 10$  ka; Shepard et al., 1995), Giggie Springs and Mizpah ( $^{40}\text{Ar}/^{39}\text{Ar}$  ages of  $<81 \pm 5$  ka and  
152 620-740 ka, respectively; Heizler, 2013) and Hi Desert basalts. Note that we infer the Giggie Springs  
153 age to be close to its 81 ka maximum based on the degree of lava surface modification. Field  
154 relationships indicate that Hi Desert basalt is older than Giggie Springs, but it is uncertain whether it  
155 predates or postdates the Mizpah eruption. The vents for the Giggie Springs, Mizpah, and Hi Desert  
156 basalts are located within ~500-600 m of each other, and allow us to assess variations between closely  
157 spaced, but different aged, volcanoes as well as potential variations within individual units. The vent  
158 for Marcath is ~6 km southeast of these three, allowing to test for variability in magmatic processes  
159 that might be related to time rather than co-location.

160

161

### 162 **Hi Desert Basalt (Qhib, age undetermined)**

163

164 The Hi Desert basalt (Figure 2) crops out as remnants of two small agglomerate cones, 10-20 m  
165 high and ~150 m diameter, that are surrounded and partly buried by later lavas and sediments. Hi  
166 Desert products are basalts to trachybasalts (Figure 3) notable in the field for the abundant euhedral  
167 plagioclase megacrysts, ~1-1.5 cm in size and rarely up to 5 cm. In thin section (neglecting  
168 megacrysts), the rock contains ~20% phenocrysts of subhedral olivine (2 and 3 mm in size), 5-10% of

169 phenocrysts of subhedral clinopyroxene (0.5 to 2 mm), and 10% euhedral plagioclase (1 to 2 mm), in a  
170 groundmass of plagioclase and ferromagnesian minerals.

171

172 **Mizpah Basalt (Qmzb; 620-740 ka)**

173

174 The Mizpah products form an elongate (~2.5 km long, ~800 m wide, 10-15 m thick) lava field  
175 with a subdued surface that extends westward from its small, 40 m-high scoria cone source (Figure 2).  
176 Mizpah rocks are trachybasalts (Figure 3) and typically porphyritic, containing < 10% subhedral  
177 olivine (0.1-0.2 mm) with sparse ~2 mm olivine phenocrysts; 5% subhedral to euhedral clinopyroxene  
178 (0.1-0.2 mm); and <10% euhedral plagioclase phenocrysts (0.3-0.6 mm) in some cases with sieve  
179 textures. The groundmass has a trachytic texture containing plagioclase and ferromagnesian minerals.

180

181 **Giggle Springs basalt (Qgsb;  $<81 \pm 5$  ka)**

182

183 Giggle Springs products consist of two tephrite/basanite lava fields (5 km and 1.6 km long, 2-5  
184 m thick; Figures 2, 3) that emanate from the ends of an agglomerate rampart (fissure vent), and partly  
185 overlie and partly surround Mizpah lava. The two Giggle Springs lava fields have moderately  
186 modified lava surfaces, where rafts of proximal agglomerate are preserved as mounds but areas  
187 between mounds have significant accumulations of eolian sediment and desert pavement. Lava levees  
188 and a drained lava channel are well preserved within a few hundred meters of the vent area.  
189 Megacrysts of olivine and clinopyroxene (up to ~2 cm) and plagioclase (up to ~1 cm) are abundant and  
190 ubiquitous in Giggle Springs products. Samples of the lavas contain (neglecting the megacrysts) <5%  
191 phenocrysts of subhedral olivine and clinopyroxene (0.1 - 0.2 mm) in an intergranular groundmass of  
192 plagioclase and ferromagnesian minerals.

193



194 **Marcath/Black Rock Basalt (Qm;  $38 \pm 10$  ka)**

195

196 Marcath volcano consists of a ~150 m high, elongate scoria/agglomerate cone with a basal  
197 diameter of  $900 \times 500$  m. The cone partly buries a >900 m-long agglomerate rampart that likely  
198 records an early fissure-fed phase of the eruption, and is open to the west where aa lavas flowed  
199 outward to form two compound lava fields as flows diverted around an older cone onto the adjacent  
200 valley floor (Figure 2). The 10-25 m-thick lava fields are 3.2 and 3 km long, and have maximum  
201 widths of 1.7 and 1.4 km, respectively. Tephra fall deposits extend south and northeast from the  
202 volcano, with thicknesses >4 m near the cone; the northeast lobe can be traced continuously up to 5 km  
203 from the vent (Johnson et al., 2014); local patches of ash suggest that it originally extended farther, but  
204 wind and water reworking have made it impossible to define the original outer edge of the deposit. The  
205 Marcath products are basanites to trachybasalts (Figure 3), ubiquitously containing centimeter-sized  
206 megacrysts of plagioclase, olivine, clinopyroxene and amphibole. Under the microscope the samples  
207 (neglecting megacrysts) are porphyritic with ~10% of phenocrysts of subhedral olivine (0.1 and 0.2  
208 mm), and ~10% of euhedral (0.1-0.3 mm) plagioclase. The groundmass is microcrystalline with  
209 microlites of plagioclase and ferromagnesian minerals.

210

211

212 **ANALYTICAL TECHNIQUES**

213

214 A suite of 24 samples (Table 1) was collected from the four units that are the focus of the study  
215 for petrography, whole-rock chemistry, mineral chemistry and geochronology. Samples were also  
216 collected for isotopic analyses (Rasoazanamparany et al., in review.). Petrography was determined  
217 using the petrographic microscope combined with the study of back-scattered electron images taken  
218 with a Hitachi S-4000 scanning electron microscope (SEM) at the University of Buffalo, equipped with

219 an energy dispersive X-ray spectrometer to qualitatively determine the composition of the main mineral  
220 phases in the samples.

221 Whole rock chemistry samples were chipped using a Bico Badger and powdered in a Bico  
222 Shatterbox for three minutes. Approximately 20 g of powdered samples were weighed in porcelain  
223 crucibles and placed in a furnace at 110 °C for two hours, cooled and weighed again, and then placed in  
224 a 1000 °C furnace for an additional 1.5 hours in order to measure the loss on ignition. For major-  
225 element analyses with x-ray fluorescence spectrometry (XRF), sample powders were mixed with a 50-  
226 50 mix of Li-tetraborate and Li-metaborate, melted, and rapidly cooled to form glass disks. The glass  
227 disks were ground on 30-micron diamond abrasion pads to expose a fresh and flat analytical surface  
228 and then cleaned with isopropanol. Sample powders were prepared for trace element analysis on the  
229 XRF by mixing 3 g of binder and 12 g sample powder. Samples were then placed on a Buehler  
230 Specimen Mount Press and pressed to pellets. A Panalytical Axios wavelength dispersive XRF was  
231 used for both major and trace element analyses at University of Nevada Las Vegas (UNLV). Elements  
232 analyzed with the glass fusion disks include SiO<sub>2</sub>, Al<sub>2</sub>O<sub>3</sub>, TiO<sub>2</sub>, Fe<sub>2</sub>O<sub>3</sub>(t), MgO, Na<sub>2</sub>O, K<sub>2</sub>O, MnO,  
233 CaO, and P<sub>2</sub>O<sub>5</sub>, all reported in weight percent. Elements analyzed with the pressed pellets include Sc,  
234 V, Ni, Cu, Ga, Rb, Sr, Y, Zr, Nb, Ba, La, Hf, Pb, Th, and U, all reported in parts per million (ppm).  
235 The detection limits for most elements is <5 ppm, except La (30 ppm) and Nb (10 ppm).

236 Rare earth elements were analyzed at Activation Laboratories in Ancaster, Ontario, using a Li-  
237 tetraborate-Li-metaborate fusion method on an ICP-MS (see [www.actlabs.com](http://www.actlabs.com) for analytical procedure  
238 and detection limits)

239 Main mineral phases were analysed using the JEOL JXA-8900 electron microprobe at UNLV  
240 and at the Cornell Center for Materials Research (CMMR) at Cornell University. Conditions of the  
241 analysis on both instruments were 15 kV current, a 5-μm beam for ferromagnesian phases, and a 10-  
242 μm beam for plagioclase. In the latter, sodium was analysed first in order to avoid loss in the counts of  
243 this element. Consistent with hand specimen and petrographic studies, important phenocrysts phases

are olivine, clinopyroxene, plagioclase and some amphibole, as well as gabbroic and ultramafic enclaves from the Marcath unit. Analyzable glass was not found in the groundmass of the samples. Melt inclusions were not detected in any mineral phases; therefore, calculations of the intrinsic conditions of the different systems are based on the equilibrium between mineral phases, rather than between mineral phases and glass (Putirka, 2008).

## ANALYTICAL DATA AND RESULTS

### Major and Trace Elements

Samples from the four volcanoes are tephrites/basanites and basalts to trachybasalts (Table 2, Figure 3) with SiO<sub>2</sub> varying from 43 to 50 wt. %, MgO from 6 to 12 wt. %, and CaO from 8 to 11 wt. %; this range occurs across the four volcanoes as well as within two of the individual volcanoes. Although the Hi Desert basalt seems to be slightly more evolved than the other units, overall no clear trends can be observed in a set of element-versus-MgO variation diagrams (Figure 4).

Rare-earth elements compared to OIB basalts strongly suggest an OIB source for the melts (Table 2, Figures 5, 6; Sun and McDonough, 1989). Slight differences in the slope of the REE plots (Figure 5) are well illustrated in a plot of La/Yb vs. Zr/Nb (Figure 7a); Marcath and Giggie Springs units are similar and relatively tightly clustered, while Hi Desert and Mizpah have broader, overlapping fields. Consistent with the main crystallizing phases (olivine, orthopyroxene, clinopyroxene), we have selected Th and Ta as incompatible elements and Cr as compatible (Table 4a) to test for degree of partial melting and further mineral fractionation of these melts. In a plot of Th/Ta vs. Cr/Ta (Figure 7a), no significant differences in the degree of fractionation (Th/Ta) of the source are observed although the figure suggests a variable degree of partial melting (Cr/Ta) in the units (Ta is slightly more incompatible than Th; Tables 4a,b). In a plot of Dy/Yb vs La/Yb (Figure 7b) to test for garnet or spinel in the source,

no clear differences in the ratio Dy/Yb are observed (~0.08 to 0.18). Following Barth et al., (2000), we have also plotted the ratio La/Nb vs Nb [ppm] (Figure 8a) and the ratio Nb/Ta vs Nb [ppm] (Figure 8b) to test for crustal contamination. Overall, the samples cluster close to the chondritic ratio although the amount of Nb is several orders of magnitude higher than the sources proposed by Barth et al. (2000).

## **Mineral Chemistry**

Olivine phenocrysts occur in all the units, both as phenocrysts and in the groundmass, and have a range of compositions from Fo<sub>57</sub> to Fo<sub>87</sub> for Hi Desert, Fo<sub>63</sub> and Fo<sub>87</sub> for Mizpah, Fo<sub>67</sub> and Fo<sub>87</sub> for Giggle Springs and for Marcath (Table 3a, Figure 9a), although intermediate-composition olivine is less abundant in Marcath units.

Clinopyroxene phenocrysts and groundmass crystals are generally less common than the olivine phase, but occur in all samples. The main pyroxene phase is diopside in Hi Desert and Mizpah samples, and both diopside and augite (based on the classification of Morimoto, 1989) in Giggle Springs and Marcath. The fact that several of the analyses plot above the diopside limit (Table 3b, Figure 9b) is due to a relatively high Al<sup>3+</sup> content in their formula, as they contain amounts of the jadeite end-member (NaAlSi<sub>2</sub>O<sub>6</sub>), equivalent to a subtle omphacitic component in clinopyroxenes from Hi Desert, Giggle Springs, and Marcath. This suggests relatively higher-pressure crystallization conditions compared to a normal Ca-Mg-Fe<sup>2+</sup> clinopyroxene (Morimoto, 1989) and requires the charge balance proposed by Papike et al., (1974) and Cameron and Papike (1981) to estimate iron speciation in the pyroxene formula.

Plagioclase (Table 3c, Figure 9c) has a relatively narrow range of labradoritic compositions in Mizpah, Giggle Springs, and Marcath rocks (An<sub>61-68</sub>, An<sub>60-69</sub>, and An<sub>57-72</sub>, respectively), with a few phenocrysts of an andesine-oligoclase-like phase (~An<sub>30</sub>). A similar andesine-oligoclase phase was observed in Hi Desert, however plagioclase phenocrysts range in composition between An<sub>48</sub> and An<sub>71</sub>;

294 a wider range than found in the other three units.

295 Amphibole was found exclusively in products from Marcath volcano as a phenocryst phase and  
296 also as the main phase of <4-cm mafic inclusions that are common around the Marcath edifice and in  
297 the proximal areas of Marcath lava flows (Figure 2). Marcath amphibole compositions vary from  
298 pargasite to magnesiohastingsite and kaersutite (Table 3d, Figure 9d) based on the Leake et al. (1997)  
299 cation allocation scheme and classification.

300

### 301 **Intrinsic conditions of crystallization**

302

303 The methods used here to calculate pressure, temperature and oxygen fugacity are based on  
304 mineral equilibria of the main crystallizing phases. There are two fundamental aspects considered in  
305 these calculations: (1) whether the pairs of mineral phases are in thermodynamic equilibrium (a non-  
306 trivial issue in volcanic rocks), and (2) how to determine one value of a given intrinsic condition, based  
307 on the calculation of such a value from a data set that is often composed of hundreds microprobe  
308 analyses.

309

310 **Thermometry.** Crystallization temperature was estimated using an olivine – clinopyroxene  
311 thermometer. There are several formulations of this equilibrium, originally developed by Powell and  
312 Powell (1974), all of them based of the interchange of Mg-Fe between olivine and augite:

313



315 ol cpx ol cpx

316

317 One of its current formulations was proposed by Loucks (1996), wherein the equilibrium constant of  
318 Equation (1) depends on temperature through a non-linear relationship that can be solved with a

numerical method. In order to assess whether the two mineral phases are in equilibrium we rely on the equilibrium window proposed by Cortés et al. (2005). In their model, since the equilibrium olivine-melt can be equated with the equilibrium clinopyroxene-melt assuming the same melt, the value of the equilibrium constant of the reaction (Equation 1) is constrained if the mineral phases are in equilibrium. According to Cortés et al. (2005) the equilibrium constant, expressed as iron-magnesium ratios, varies between 0.64 and 1.88 with a mean of 1.22. We also rely on the petrography of the samples and assume that equilibrium is attained between two mineral phases in physical contact, although the calculation is not performed on analyses on the interface between the two grains, to avoid Ostwald ripening and elemental diffusion issues between the involved phases.

The composition of each mineral phase in Equation 1, using a large number of analyses, should be normally distributed due to the inherent randomness in crystallization. Because expressing the free energy at equilibrium *implies the calculation of a ratio* between two random variables in which each follow a normal distribution (e.g. the chemical analyses of the mineral phases), the result of the calculation will be a random variable that follows a Cauchy-Lorentz distribution. Since the expected value and variance of a Cauchy-Lorentz distribution are undefined, the best estimation of a measure of central tendency is the median while half the sample interquartile range (HIQR) is a robust estimator of the spread of the statistical sample (e.g. all the calculations performed). The procedure is then used to first calculate all the possible outcomes of temperature for mineral pairs that are assumed in equilibrium, and then to select the median and HIQR of the calculated temperatures. Resulting crystallization temperatures for Hi Desert and Mizpah rocks are between 1050-1100°C, compared to 900-1050°C for the younger Giggie Springs and Marcath units.

**Pressure.** The lack of glass also precludes crystallization geobarometric calculations based upon melt-mineral phase equilibrium (e.g., clinopyroxene-melt; Putirka, 2008). Nimis and Ulmer

(1998) and Nimis (1999) suggest an alternative geobarometer that is based on the structural lattice of clinopyroxene formed in equilibrium with a basaltic melt, such that its composition is not explicitly needed. This geobarometer is relatively insensitive to temperature in alkaline compositions such as those studied here. Because the calculation is performed directly from the composition of clinopyroxene, it is desirable that the distribution of pressures follows a normal distribution if there is one population of clinopyroxene. With this condition, it is straightforward to calculate the mean and standard deviation of the pressure values. Calculated Hi Desert and Mizpah crystallization pressures range between 0.9-1.3 GPa (~30-45 km). The younger units (Giggle Springs and Marcath) have bimodal crystallization pressures with values between 1-1.3 GPa and between 0.3-0.6 GPa (~35-45 km and 10-20 km, respectively).

Empirical observations of amphiboles from calc-alkaline intrusions (Hammarstron and Zen, 1986) show that the amount of total aluminium in amphiboles is proportional to pressure of crystallization (see Ridolfi et al., 2010, for a summary of the different calibrations). Recently, Ridolfi and Renzulli (2012) and Simakin et al. (2012a) have extended the original calibration to mafic products and mafic enclaves, however more work remains to be done in order to have a robust geobarometer based on this mineral phase. The accuracy of the Ridolfi et al. (2010) geobarometer is  $\pm 0.3$  GPa (Simakin, pers. comm.) while the Simakin et al., (2012a) model has an accuracy of  $\pm 0.05$  GPa. We applied the Ridolfi and Renzulli (2012) model to a set of amphibole phenocrysts found in mafic inclusions within the Marcath lava flow (Table 3d). According to this model, crystallization pressures vary between 0.69-0.75 GPa, overlapping the lower range of values of the clinopyroxene-based crystallization pressures described above. On the other hand, the Simakin et al., (2012a) model did not produce meaningful results in our analyses (negative values), hence we favour the Ridolfi and Renzulli (2012) model, conscious that it is an over-estimation of the pressure with an error of ~25%. The Ridolfi and Renzulli (2012) model also provides temperature estimates between 1037-1070 °C (consistent with the olivine-clinopyroxene-based crystallization temperatures stated above, taking into account the large

error in the calculation), oxygen fugacity between  $\Delta\text{NNO} -0.2$  and  $\Delta\text{NNO} +0.5$ , and estimated water content in the melt between 5-7 wt%. This range of water content is comparable to those estimated for trachybasalts in the Southwest Nevada Volcanic Field, the nearest Quaternary volcanic field, ~200 km to the south (Nicholis and Rutherford, 2004), and with the higher part of the water content range determined for the Big Pine field, ~250 km west-southwest of LCVF (Gazel et al., 2012).

**Oxygen fugacity.** Oxygen fugacity estimates are based on the speciation of iron in the clinopyroxene unit formula (Cortés et al., 2006, Simakin et al., 2012b). If the speciation of iron in the clinopyroxene is not known (as it is always the case from a typical electron microprobe analysis), such speciation is calculated based on the charge balance proposed by Papike et al., (1974) and Cameron and Papike (1981). The calculation must also include the contribution of elements such as Na, Ti,  $\text{Fe}^{3+}$  and Cr, which are not considered in the pyroxene quadrilateral. The intrinsic oxygen fugacity of the system is then estimated assuming equilibrium between the clinopyroxene formula and the melt, although the composition of the melt is not directly needed for the calculation (Cortés et al., 2006). If the temperature is calculated using an independent method, it is possible to additionally determine the absolute oxygen fugacity of the system. As with the barometry described above, one population of clinopyroxene phenocrysts ought to produce values of intrinsic oxygen fugacity that are normally distributed. Cortés et al. (2006) estimated that this approach has a sensitivity of  $\pm 1$  QFM unit.

Oxygen fugacity calculations using both Cortés et al. (2006) and Simakin et al. (2012b) methods give comparable values of the oxidation state in the samples. For the older units (Hi Desert and Mizpah) intrinsic oxygen fugacity relative to QFM buffer is estimated between  $\Delta\text{NNO}+2$  and  $\Delta\text{NNO}+4$ . For the younger magmas (Giggle Springs and Marcath) are relatively reduced with values of intrinsic fugacity between  $\Delta\text{NNO}+1$  and  $\Delta\text{NNO}+2$ , comparable with amphibole oxygen geobarometry results.



### **Depth of partial melting and origin of the basaltic melts.**

Depths of partial melting were estimated using two approaches: a silica-melt barometer (Lee et al., 2009), and an orthopyroxene-liquid geobarometer (Putirka, 2008); both calculations are performed using the whole-rock composition of the basaltic products as a proxy of the equilibrium melt. The Lee et al. (2009) technique applies a silica-based barometer that is based solely on the activity of silica in the melt. As a result, it is more reliable and less sensitive to incompatible element variability and mantle composition than earlier barometers (e.g. Wang et al., 2001). The Lee et al. (2009) barometer was calibrated using 433 basalt compositions in equilibrium with olivine and orthopyroxene over a range of temperatures from 1110 to 1800 °C and pressures of 1 atmosphere to 7 GPa. Barometer calibration yielded an uncertainty of  $\pm 0.20$  GPa (Lee et al., 2009). The thermometer generated is consistent with the barometer and has an uncertainty of  $\pm 3\%$  (Lee et al., 2009). When using this barometer, it is critical that the primary magma contains both olivine and pyroxene. Further, the barometer is not calibrated for silica-undersaturated rocks with  $< 40$  wt. %  $\text{SiO}_2$ , and it is best to choose the most primitive basalt with  $\text{MgO} > 8.0$  wt.% for pressure and temperature calculations.

The orthopyroxene-barometer (Putirka, 2008) is calibrated for basalts with  $\text{SiO}_2$  contents as low as 35 wt. %, will work for basalt with olivine and both clinopyroxene and orthopyroxene, and is independent of source composition (as long as pyroxene and olivine are in equilibrium with the source at the time of partial melting). Using clinopyroxene + olivine results in almost no increased error relative to olivine + orthopyroxene (Putirka et al., 2012).

Using the method of Lee et al. (2009) in the most primitive whole-rock chemical analyses from our dataset produces temperatures of partial melting of the mantle of the order of 1500-1700°C with pressures between 3-6 GPa, which, for an average density of  $\sim 3000 \text{ kg/m}^3$ , implies depths of the partial melting between  $\sim 100$ -200 km. The Putirka (2008) calibration indicates that partial melting occurred at temperatures ranging from 1460 to 1650 °C and pressures between 1.7-3.8 GPa, which implies depths of  $\sim 60$ -130 km, consistent with the depth of the asthenospheric mantle in the region (e.g. Fisher et al.,

418 2010; Kumar et al., 2012).

419 An important caveat for the Lee et al. (2009) approach is that to apply the model, the source  
420 rock is assumed to be a peridotite. In order to assess this condition for the magmas of interest here, we  
421 estimate the mineralogy of the mantle sources based on olivine mineralogy (Sobolev et al., 2000). In  
422 Figure 10a, we plotted  $\text{Fe}^{2+}/\text{Mn}$  in olivine vs. %Fo, while in Figure 10b we plotted  $100\times\text{Ca}/\text{Fe}^{2+}$  vs  
423  $100\times\text{Mn}/\text{Fe}^{2+}$  for the olivine analyses with %Fo > 85, following Sobolev et al. (2007). Based on these  
424 plots, we conclude that the most likely source for these magmas has a modal mineralogy that lies  
425 between the pyroxenite and peridotite (lherzolite) fields as defined by Sobolev et al. (2007), although  
426 nickel content in olivine reported by Sobolev et al., (2007) is higher compared with LCVF olivine.  
427 Source identification based on olivine composition is consistent with the approach of Hirschmann  
428 (2000) and Petermann and Hirschmann (2003) based on the whole-rock composition, because  
429  $\text{FeO}/\text{MnO}_{(\text{melt})}$  is proportional to the ratio  $\text{Fe}^{2+}/\text{Mn}_{(\text{ol})}$ . Thus because the Lee et al. (2009) method  
430 assumes a peridotite source, Putirka's (2008) method, which can be applied to a variety of sources as  
431 long as they are olivine and pyroxene saturated is favored here.

432

433 **MELTS modelling.** Geothermometry and geobarometry calculations were compared with the  
434 MELTS and pMELTS thermodynamic models (Ghiorso and Sack, 1995; Asimow and Ghiorso, 1998;  
435 Ghiorso et al., 2002) as a preliminary, but rough validation, since the LCVF conditions are indeed  
436 beyond the working limits defined by Ghiorso et al. (2002). We specifically aimed for a preliminary  
437 estimation of liquidus temperatures at the calculated pressures by the silica activity barometer, and at  
438 the crystallization pressures calculated using the clinopyroxene barometer described above. We also  
439 used these thermodynamic models to estimate the potential crystallizing mineralogy to compare with  
440 products of the four volcanoes. No calculations of the liquid line of descent were performed because  
441 evolved magmas are not present at Lunar Crater. Instead, compositions cluster around  $\text{SiO}_2 \sim 44\text{-}46$   
442 wt%.

Liquidus temperatures at the pressures of interest were calculated for the most primitive sample of our dataset (sample LC10-20; SiO<sub>2</sub> = 44.02 wt%; Table 5), as well as, for comparison, for a reference pyroxenite sample (Table 2) from the Earth Reference database (<http://earthref.org>); oxygen fugacity  $\Delta QFM+2$  was assumed in both cases in order to constrain the iron speciation in the samples, and 2% of H<sub>2</sub>O was assumed in sample LC10-20 consistent with a conservative “wet” liquidus. The temperatures predicted using the Lee et al. (2009) or Putirka (2008) models are comparable to pMELTS-calculated liquidus temperatures (1584°C-1664°C) for both the basalt and pyroxenite given estimated partial melting pressures not higher than 3.8 GPa. The pMELTS model also predicts that the crystallizing phases at 35-45 km depth (equivalent to the crystallization pressures calculated above for Mizpah and Hi Desert, and the deeper of two crystallization pressures that were calculated for Giggle Springs and Marcath) are plagioclase, olivine, clinopyroxene, and orthopyroxene, as well as amphibole and biotite. Except for biotite, all these phases were observed in the volcanic products.

#### **Crystal Size Distribution (CSD)**

Crystal size distributions (CSD; Marsh, 1988, 1998; Higgins, 2006) of olivine, clinopyroxene, and plagioclase were measured from back-scattered electron images of samples from the Mizpah, Giggle Spring and Marcath units. Note that olivine CSD was not measured for Marcath products because olivine is rare in these units (Figure 10a). Images were imported into ImageJ freeware (<http://rsb.info.nih.gov/ij/>) in which long and short axes of the different mineral phases were measured; a total of 200 measurements were performed on each mineral phase in order to have a representative sample of each CSD (Mock and Jerram, 2005; Morgan and Jerram, 2006). Mean crystal aspect ratios were determined using the CSDSlice method (Morgan and Jerram, 2006), fabric was considered massive (e.g. with no foliation), and measurements were not corrected for crystal roundness. All these values as well as the measurements were exported into CSDCorrections 1.4 (Higgins, 2006) in order to

468 calculate the crystal size distribution of each mineral phase. The total slide area, volumetric phase  
469 abundance and vesicularity of the samples were determined using built-in features of ImageJ and  
470 estimated from the petrography of the samples.

471 Proximal products of Giggle Springs volcano have smaller sizes than the more distal lava, and  
472 there is a partial overlap of the CSDs of the main phenocryst phases although groundmass CSDs are  
473 different. The CSD of the olivine phase in Giggle Springs and Mizpah has an inflexion point in the  
474 distribution at approximately 0.1 mm for some samples (Figure 11a); olivine phenocrysts in both units  
475 have similar distributions except at the smallest sizes. The slope of the CSD of olivine phenocrysts is ~  
476  $-16 \text{ [mm}^{-4}]$  ( $r^2 \sim 0.96$ ) and  $\sim -58 \text{ [mm}^{-4}]$  ( $r^2 \sim 0.95$ ) for groundmass microlites (cut off at 0.1 mm),  
477 suggesting residence time of few hours for the phenocrysts using growth rates of 0.2-0.4 mm per day  
478 reported for olivines in Hawaiian tholeiites (Maaløe, 2011).

479 The clinopyroxene CSDs (Figure 11b) are similar between samples from Giggle Springs and  
480 Mizpah, but different from Marcath samples, which has consistently larger crystals. The plagioclase  
481 CSDs for the different units agree in an intermediate range of sizes between  $\sim 0.1$  and  $\sim 0.3$ . While this  
482 is the upper range for Giggle Springs and Mizpah, it is the lower range for the samples from Marcath  
483 (Figure 11c). Oxides (Figure 11d) are substantially different in all the samples (even those from the  
484 same unit), suggesting late crystallization events.

485

486

## DISCUSSION

### 487 *Melting depths and source composition*

488 Independent of the age and location of the four studied volcanoes, the geochemical data  
489 strongly indicate sources located in the asthenosphere, at depths between 60 and 130 km based on the  
490 Putirka (2008) orthopyroxene barometer. Considering  $\text{Fe}^{2+}/\text{Mn}$  and  $\text{Ca}/\text{Mg}$  in olivine phenocrysts with  
491  $\% \text{Fo} > 85$ , the source material is likely to have a modal mineralogy between pyroxenite and peridotite  
492 (Petermann and Hirschmann, 2003; Tuff et al., 2005; Sobolev et al., 2007; Herzberg, 2011). The most

likely source is an olivine websterite, although the nickel content in the LCVF olivine is lower (less than 2000 ppm) than the reported values by Sobolev et al., (2007) for pyroxenite or peridotite (between 2000 and 4000 ppm). The lower concentration of nickel in olivine suggests a low-Ni source (Herzberg, et al., 2013), although Ni content in whole-rock analyses is within reasonable values (120 to 330 ppm). A possible explanation for this difference might be related to the oxidation state of the magmas. Oxidation state of the depleted and enriched mantle is thought to be close to QFM and NNO+1 respectively (Balhaus, 1993). Our estimation of the oxygen fugacity by the clinopyroxene and amphibole formulas seems to indicate more oxidizing conditions for these basalts thus implying changes in oxygen fugacity during ascent and the main crystallization event. The more oxidizing conditions might have affected  $\text{Ni}^{3+}$  concentrations in the basaltic melt, a species that cannot enter in the olivine formula due to its charge, although the specific relation of the oxygen fugacity and the speciation of nickel is not yet completely understood. A plausible explanation for the more oxidizing conditions during crystallization is likely to be related to the water content of these magmas. The presence of amphibole seems to indicate a relatively high amount of water, which, depending on its speciation, has been linked to changes in the oxidation state of melts (e.g. Barker and Rutherford, 1996).

Rare-earth element ratios are helpful for estimating the depth of partial melting as well as the mineralogy and chemistry of the source, because of the different solid/melt distributions of REE in spinel vs. garnet bearing peridotite/pyroxenite. Heavy rare-earth elements like Yb are highly compatible in garnet while light-rare earth elements like La are incompatible; therefore partial melting of peridotite or pyroxenite containing garnet will produce melts with high La/Yb. Variable degrees of partial melting will result in changes in La/Yb such that the higher degree of melting, the lower La/Yb. Further, middle-rare earth element (MREE)-heavy rare earth element (HREE) ratios are sensitive to whether garnet exists as a residual phase in the source, because HREEs like Yb are retained by garnet during a melting event. This produces large changes in MREE/HREE in magmas generated by melting

518 of a garnet-bearing source, a change that is especially prominent with larger degrees of partial melting.  
519 Garnet is a relatively refractory mineral and does not significantly contribute to the melt phase until  
520 larger degrees of melting. At small melt fractions, melting of olivine or pyroxene results in little to no  
521 change in in MREE/HREE (Dy/Tb) because of similar partition coefficients for Dy and Tb in olivine  
522 and pyroxene (e.g.,  $D_{\text{Dy}}/D_{\text{Yb}}=0.75$  to 1.5 for clinopyroxene; Chazot et al, 1996). This results in  
523 melting trajectories that are relatively flat (or with slightly decreasing Dy/Yb) until about 30% melting.  
524 For higher degrees of melting, Dy/Yb decreases rapidly as garnet is melted. In the case of the Lunar  
525 Crater volcanoes La/Yb varies from 3 to 15 with the higher ratios suggesting a garnet source (Figures  
526 7a,c, 12a,b). The mode of a typical garnet lherzolite is 60% olivine, 20% orthopyroxene, 8%  
527 clinopyroxene and 12% garnet (Thirwall et al, 1994). This source produces melts that are too high in  
528 Dy/Yb to match Lunar Crater magmas (Figure 12a). If, however, garnet is not as abundant in the  
529 source (5 to 8%), modelled melts provide a much better match to the sample set. We also modelled the  
530 melting of a spinel lherzolite with 57.8% olivine, 27% orthopyroxene, 11.9% clinopyroxene and 3.3%  
531 spinel. Although this source produced melts with relatively constant Dy/Yb, the value of the ratio was  
532 much to low to match the dataset. Based on Figure 10b and following Sobolev et al., (2007), we have  
533 also modelled the source as an olivine websterite (i.e. a composition between lherzolite and pyroxenite)  
534 with 30-35% olivine, 30-40% orthopyroxene, 20-30% clinopyroxene, and 5-11% garnet (Table 4b).  
535 Results using this source are similar to the lherzolite models (Figure 12b) except that the final melt has  
536 a lower Dy/Yb. Our conclusion is that the source of Lunar Crater magma has a composition between a  
537 garnet lherzolite and an olivine websterite containing 5 to 8% garnet. Consistency between this result  
538 and that of the independent method based upon olivine  $\text{Fe}^{2+}/\text{Mn}$  and  $100\text{xCa}/\text{Mg}$  ratios reinforces this  
539 interpretation. Note that we did not calculate major element models involving partial melting because  
540 of the sensitivity of melt chemistry to source composition. Meaningful major element models would  
541 require knowledge of major element chemistry of the source. This information is at present not known  
542 well enough for Lunar Crater.

543

## 544 *Magma evolution*

545         The variation of Th/Ta is used here to determine the degree of fractionation because both  
546 elements are incompatible, however Ta is more incompatible than Th (Table 4b) while Cr/Ta varies  
547 with different degrees of partial melting in a source containing an olivine websterite component (Cr is  
548 highly compatible in both ortho- and clinopyroxene). The narrow range of Th/Ta values relative to  
549 Cr/Ta (Figure 7b) indicates variable differences in the degree of partial melting within units, while the  
550 trace element variability (e.g., Figure 6) is consistent with small variations in source composition. On  
551 the other hand, there is little evidence for systematic fractionation processes in the resulting magma  
552 batches as evidenced by nearly constant Th/Ta ratios (Figure 7b).

553         In order to generate the basaltic compositions similar to those reported in Table 2, the required  
554 amount of partial melting of a olivine websterite/lherzolite source is ~3-5% based on the batch model  
555 calculations presented in Figures 12a,b.

556

## 557 *Source Heterogeneity*

558         Source heterogeneity is evident between different, but closely spaced, volcanoes (e.g., Giggie  
559 Springs compared to Hi Desert; Figure 7a) and within individual volcanoes (e.g., Mizpah, and possibly  
560 Hi Desert). The spatial scale of subtle mantle variability must be similar to the scale of the partial melt  
561 domains tapped by the older Hi Desert and Mizpah feeding systems. These observations suggest lateral  
562 length scales of ~500 m or less for compositional heterogeneity in the source, if the magmas were  
563 sourced at similar depths. In contrast, the two younger volcanoes (Giggie Springs and Marcath) had  
564 essentially identical sources based upon the data presented here, even though the volcanoes are ~6 km  
565 apart and have age differences of several tens of thousands of years; furthermore, their sources were  
566 homogeneous on the scale of the individually tapped melt domains. We realize that melts can travel  
567 laterally from source to surface, implying that in some cases, source areas may not lie directly below

568 vents. If this is the case for the northern Lunar Crater volcanoes, our stated spatial scale of source  
569 heterogeneity should be regarded as a minimum estimate. Figures 8a,b suggest that although the  
570 samples are close to chondritic Nb/Ta and La/Nb, Nb [ppm] is several order of magnitude higher than  
571 the mantle or the upper crust and is especially enriched in the younger units (up to 90 ppm in Marcath).  
572 This result strongly suggests the addition of an additional crustal (oceanic) component. Isotopic data  
573 (Sr Nd Pb, Hf and Os) also indicate a heterogeneous source over very small spatial scales, likely related  
574 to ancient subduction processes and consistent with our interpretation (Rasoazanamparany et al. in  
575 review).

576

#### 577 ***Magma Ascent and lithospheric contamination***

578 Crystallization occurred at depths of 30-45 km beneath the four volcanoes, with additional  
579 crystallization at 10-20 km for the two younger units. Crustal thickness in the area is estimated at 30-  
580 35 km (Gilbert and Sheehan, 2004). Thus, enriched melts generated in the asthenospheric mantle  
581 travelled relatively unimpeded to near or just beneath the base of the crust, where all four magma  
582 batches ponded and underwent up to 50% crystallization as determined from MELTS modelling. The  
583 intrinsic variables and the lack of evidence for crustal contamination (Rasoazanamparany et al., in  
584 review) indicate that magmas feeding the two older volcanoes, Mizpah and Giggle Springs, ascended  
585 rapidly from near the base of the crust to the surface without intermediate ponding.

586 In contrast, the younger Giggle Springs and Marcath magmas apparently stalled at mid-crustal  
587 depths and underwent further crystallization. Fundamental differences in the CSD of their main mineral  
588 phases suggest that their mid-crustal reservoirs were not connected to each other, which is also  
589 consistent with the likely age difference between the two ( $38 \pm 10$  ka and  $81 \pm 5$  ka for Marcath and  
590 Giggle Springs,  $\sim 620$ -740 ka for Mizpah). Amphibole crystallized in Marcath's crustal reservoir, and is  
591 present in the eruptive products as megacrysts. This phase has only been observed at Marcath, implying  
592 either that: (1) there was a slight difference between the crystallization conditions of Marcath and



593 Giggle Springs such as higher water content in the former, while pressure, temperature and oxygen  
594 fugacity were similar; or (2) that the amphibole efficiently separated from or was completely  
595 assimilated by the soon-to-be-erupted Giggle Springs magma. Arguing against complete assimilation  
596 is the observation that resorption of >1 cm amphiboles during the short time scale of final ascent might  
597 not be feasible. Mafic enclaves at both Marcath and Giggle Springs volcanoes likely represent  
598 crystallization products of these or other ponded magma batches that had not yet solidified; in the latter  
599 case, temporary stalling allowed for thermal and chemical interactions that facilitated entrainment of  
600 the enclaves (e.g., Valentine and Hirano, 2010).

601 Despite the mid-crustal ponding of Giggle Springs and Marcath magmas, the lack of evidence  
602 of crustal contamination (supported both by the major and trace element chemistry, and by isotopic  
603 data; Rasoazanamparany et al., in review) indicates that ascent between storage levels, and between the  
604 crustal reservoir and the surface, was rapid. Rapid ascent is a common feature of intraplate, small  
605 volume alkali-basalt volcanoes (e.g., Luhr et al., 1995; Valentine and Perry, 2007; Smith et al., 2008;  
606 Muffler et al., 2011). The lack of contamination, even though the magma did pond in the mid-crust, is  
607 consistent with the volcanoes being fed by small, single batches of magma. When a small batch of  
608 magma ponds it is expected that the margins will rapidly chill, increasing in local viscosity and  
609 potentially solidifying. This isolates of the inner part of the intrusion from country rocks both  
610 chemically and mechanically, until crystallization causes the volatile content to increase sufficiently in  
611 the melt to drive dike propagation and final magma ascent to the surface. In contrast, relatively large  
612 and repeated magma batches might convect vigorously and retard development of a thick chilled  
613 margin and provide enough heat to partly melt and assimilate wall rocks.

614 An alternative explanation of the deeper-derived phenocrysts is that the Giggle Springs and  
615 Marcath magmas did not stall at the deeper 30-45 km level, but simply entrained crystals from that  
616 depth that had formed during ponding of earlier (e.g., Mizpah, Hi Desert) magmas. We view this as  
617 unlikely because if younger magmas were entraining material as they migrated upwards we would

618 expect them to sample a variety of upper mantle and crustal rocks, not just the products of earlier  
619 magma batches.

620 The final stage on the evolution of these volcanic products is eruption after the ponded magmas  
621 have crystallized olivine, clinopyroxene, plagioclase and traces of amphibole. The composition of the  
622 amphibole crystals (kaersutite to pargasite/magnesiohastingsite) and its stability suggest that this phase  
623 is derived either from a metasomatized lithospheric mantle or crystallized from an alkaline melt  
624 derived from a peridotite + olivine websterite source (Mayer et al., 2014). Our data are consistent with  
625 the latter, phenocrystic origin, for this phase.

626 The CSDs of one the younger volcanic products (Giggle Springs lava) suggest short crustal  
627 residence time, and the further crystallization and growth of olivine, clinopyroxene and an oxide phase,  
628 during eruption. Most of the samples have well developed groundmasses rather than glassy matrixes,  
629 indicating that subsolidus temperatures were reached slowly after the lava was emplaced in its final  
630 location.

631

632

## 633 **IMPLICATIONS**

634

635 The original motivation for this study was to address two questions: (1) *what are the*  
636 *compositional variability and magma ascent processes within the time span of an individual eruption?*

637 The results presented here indicate two main behaviors of the four studied volcanoes. Individual  
638 magma batches were fed by slightly heterogeneous source material for the two older volcanoes, but the  
639 younger of the two volcanoes' source rocks were relatively homogeneous even over distances of  
640 several kilometres and time differences of tens of thousands of years. Each magma batch stalled and  
641 crystallized in the uppermost several kilometres of the mantle near the base of the crust. Even for the  
642 closely spaced volcanoes (Mizpah, Hi Desert, and Giggle Springs), the age differences of 10s to 100s

643 ka and lack of substantial fractionation suggest that each magma batch and temporary deep reservoir  
644 was a separate entity rather than part of a continuous long-lived reservoir. Magmas feeding the  
645 Marcath and Giggle Springs volcanoes also stalled at mid-crustal levels. From the evidence at hand it  
646 appears that ascent rates from source to storage levels, and from final storage to eruption, were relative  
647 rapid with no geochemical interaction with surrounding rocks. (2) *What is the variability between very*  
648 *closely spaced volcanoes with different ages?* The Mizpah and Hi Desert magmas have subtle  
649 compositional variability, but time is a major factor as well. Volcanoes erupted within certain time  
650 windows (an older time window for Mizpah and Hi Desert, and a younger 0-100 ka window for Giggle  
651 Springs and Marcath) have similar source characteristics and ascent processes whether they are located  
652 within a few hundred meters of each other or are separated by many kilometres. If each monogenetic  
653 volcano is fed by a single small-volume batch of magma, with source and feeder system length scales  
654 on the order of hundreds of meters to a few kilometres (e.g., Valentine and Perry, 2006, 2007;  
655 Valentine and Keating, 2007; Brenna et al., 2012), it is not clear why volcanoes that are several  
656 kilometres and tens of thousands of years apart would have such similar magma dynamics.  
657 Preliminary data from other parts of the Lunar Crater Volcanic Field are suggesting that this time  
658 window-dependent behavior might be general over larger distances; testing this and developing a field-  
659 scale conceptual model are topics of current research.

660

661

662

## ACKNOWLEDGEMENTS

663 The authors acknowledge the editorial management of Thomas Shea and the reviews of Alexander  
664 Simakin, Cin-Ty Lee and an anonymous reviewer, whose suggestions substantially improved this  
665 paper. Discussions with Keith Putirka greatly improved the depth of melting section of the paper. This  
666 work was supported by the U.S. National Science Foundation through grant 1016100.

667

## REFERENCES

- Asimow, P.D., and Ghiorso, M.S., (1998) Algorithmic Modifications Extending MELTS to Calculate Subsolidus Phase Relations. *American Mineralogist*, 83, 1127-1131.
- Baker, L., Rutherford, M.J., (1996) The effect of dissolved water on the oxidation state of silicic melts. *Geochimica et Cosmochimica Acta*, 60, 2179-2187
- Balhaus, C., (1993) Redox states of lithospheric and asthenospheric upper mantle. *Contributions to Mineralogy and Petrology*. 114:331-348.
- Barth, M.G., McDonough, W.F., Rudnick, R.L. (2000) Tracking the budget of Nb and Ta in the continental crust. *Chemical Geology*, 165, 197-213.
- Bergman, S., Foland, K., and Spera, F. (1981) On the origin of the amphibole-rich vein in a peridotite inclusion from the Lunar Crater Volcanic Field, Nevada, U.S.A. *Earth Planetary Science Letters*, 56, 343-361.
- Bergman, S.C., (1982) Petrogenetic aspects of the alkali basaltic lavas and included megacrysts and nodules from the Lunar Crater Volcanic Field, Nevada, U.S.A. Ph.D. dissertation, Ohio State University, Columbus, Ohio.
- Brenna, M., Cronin, S.J., Smith, I.E., Sohn, Y.K., and Németh, K., (2010) Mechanisms driving polymagmatic activity at a monogenetic volcano, Udo, Jeju Island, South Korea. *Contributions to Mineralogy and Petrology*, 160, 931-950.

693

694 Brenna, M., Cronin, S.J., Smith, I.E.M., Maas, R., and Sohn, Y.K., (2012) How small-volume basaltic  
695 magmatic systems develop: a case study from the Jeju Island Volcanic Field, Korea. *Journal of*  
696 *Petrology*, 53, 985-1018.

697

698 Brown, B., Bursik, M., Deming, J., Louros, M., Martos, A., and Stine, S., (2010) Eruption chronology  
699 and petrologic reconstruction of the ca. 8500 yr B.P. eruption of Red Cones, southern Inyo chain,  
700 California. *Geological Society of America Bulletin*, 122, 1401-1422.

701

702 Brown, R.J., and Valentine, G.A., (2013) Physical characteristics of kimberlite and basaltic intraplate  
703 volcanism and implications of a biased kimberlite record. *Geological Society of America Bulletin*,  
704 125, 1224-1238.

705

706 Cameron, M., and Papike, J.J., (1981) Structural and chemical variations in pyroxenes. *American*  
707 *Mineralogist*, 66, 1-50.

708

709 Chazot, G., Menzies, M.A. and Harte, B. (1996) Determination of partition coefficients between  
710 apatite, clinopyroxene, amphibole, and melt in natural spinel lherzolites from Yemen: Implications for  
711 wet melting of the lithospheric mantle. *Geochimica et Cosmochimica Acta*, 60, 423-437.

712

713 Connor, C.B., and Conway, F.M., (2000) Basaltic volcanic fields. *Encyclopedia of Volcanoes*,  
714 Academic Press, New York, pp. 331-343.

715

716 Cortés, J. A., Wilson, M., Condliffe, E., Francalanci, L., and Cherkoff, D.G., (2005) The evolution of  
717 the magmatic system of Stromboli Volcano during the Vancori period (26-13.8 ky). *Journal of*

718 Volcanology and Geothermal Research, 147, 1-38.

719

720 Cortés, J.A., Wilson, M., Condliffe, E., and Francalanci, L., (2006) The occurrence of forsterite and  
 721 highly oxidising conditions in basaltic lavas from Stromboli volcano. Italy. Journal of Petrology, 47,  
 722 1345-1373.

723

724 Cortés, J.A., and Palma, J.L., (2012) PetrologicalINput - Graphical oUtput.  
 725 <https://vhub.org/resources/pingu>.

726

727 Deer, W.A., Howie, R.A., and Zussman, J., (1996) An Introduction to the Rock-Forming Minerals (2<sup>nd</sup>  
 728 Edition). 712 p, Pearson Education Limited, Essex, England.

729

730 Dickson, L.D., (1997) Volcanology and geochemistry of Pliocene and Quaternary basalts on Citadel  
 731 Mountain, Lunar Crater Volcanic Field, Pancake Range, Nevada. M.S. Thesis, University of Nevada  
 732 Las Vegas.

733

734 Erlund, E.J., Cashman, K.V., Wallace, P.J., Pioli, L., Rosi, M., Johnson, E., Delgado-Granados, H.,  
 735 (2009) Compositional evolution of magma from Parícutín volcano, México. Journal of Volcanology  
 736 and Geothermal Research, 197, 167-187.

737

738 Farmer, G.L., Perry, F.V., Semken, S., Crowe, B., Curtis, D., and DePaolo, D.J., (1989)  
 739 Isotopic evidence on the structure and origin of subcontinental lithospheric mantle  
 740 in southern Nevada. Journal of Geophysical Research, 94, 7885-7898.

741

742 Foland, K.A., and Bergman, S.C., (1992) Temporal and spatial distribution of basaltic volcanism in the

743 Pancake and Reveille Ranges north of Yucca Mountain. Proceedings International Nuclear Waste  
 744 Symposium, 2, American Nuclear Society and American Society of Civil Engineers, 2366-2371.  
 745  
 746 Gazel, E., Plank, T., Forsyth, D.W., Bendersky, C., Lee, C.-T. A., and Hauri, E.H., (2012)  
 747 Lithospheric versus asthenospheric mantle sources at the Big Pine Volcanic Field, California.  
 748 Geochemistry Geophysics Geosystems, 13, Q0AK06, doi:10.1029/2012GC004060.  
 749  
 750 Gilbert, H.J. and Sheehan, A.F. (2004) Images of crustal variations in the intermountain west. Journal  
 751 of Geophysical Research, 109, B03306. doi:10.1029/2003JB002730.  
 752  
 753 Ghiorso, M. S., and Sack, R. O., (1995) Chemical Mass Transfer in Magmatic Processes. IV. A  
 754 Revised and Internally Consistent Thermodynamic Model for the Interpolation and Extrapolation of  
 755 Liquid-Solid Equilibria in Magmatic Systems at Elevated Temperatures and Pressures. Contributions to  
 756 Mineralogy and Petrology, 119, 197-212.  
 757  
 758 Ghiorso, M. S., Hirschmann, M.M., Reiners, P.W., and Kress, V.C., (2002) The pMELTS: A revision  
 759 of MELTS aimed at improving calculation of phase relations and major element partitioning involved  
 760 in partial melting of the mantle at pressures up to 3 GPa. Geochemistry, Geophysics, Geosystems, 3,  
 761 10.1029/2001GC000217.  
 762  
 763 Hammarstrom, J.M., and Zen, E.A., (1986) Aluminium in hornblende—an empirical igneous  
 764 geobarometer. American Mineralogist, 71, 1297–1313.  
 765  
 766 Heizler, M.T., (2013)  $^{40}\text{Ar}/^{39}\text{Ar}$  geochronology results for Lunar Crater Volcanic Field basalts, Nevada.  
 767 New Mexico Geochronological Research Laboratory Report NMGRL-IR-792.

768 <https://vhub.org/resources/2503>.

769

770 Herzberg, C., (2011) Identification of Source Lithology in the Hawaiian and Canary Islands:  
771 Implications for Origins. *Journal of Petrology*, 52, 113-146.

772

773 Herzberg, C., Asimow, P.D., Ionov, D.A., Vidito, C., Jackson, M.G., Geist, D. (2013) Nickel and  
774 helium evidence for melt above the core-mantle boundary. *Nature*, 493, 393-397.

775

776 Higgins, M. D., (2006) Quantitative Textural Measurements in Igneous and Metamorphic Petrology.  
777 276 p. Cambridge University Press.

778

779 Hintz, A. R., and Valentine, G. A., (2012) Complex plumbing of monogenetic scoria cones: New  
780 insights from the Lunar Crater Volcanic Field (Nevada, USA). *Journal of Volcanology and Geothermal*  
781 *Research*, 239-240, 19-32.

782

783 Hirschmann, (2000) Mantle solidus: experimental constraints and the effect of peridotite composition.  
784 *Geochemistry, Geophysics, Geosystems*, 1, doi: 10.1029/2000GC000070.

785

786 Johnson, P., Valentine, G.A., Cortés, J.A., Tadini, A. (2014) Basaltic tephra from monogenetic  
787 Marcath Volcano, central Nevada. *Journal of Volcanology and Geothermal Research*, 281, 27-33.

788

789 Johnson, E.R., Wallace, P.J., Cashman, K.V., Delgado Granados, H., and Kent, A.J.R., (2008)  
790 Magmatic volatile contents and degassing-induced crystallization at Volcán Jorullo, Mexico:  
791 implications for melt evolution and the plumbing systems of monogenetic volcanoes. *Earth and*  
792 *Planetary Science Letters*, 269, 478-487.



793

794 Kargel, (1986) The geochemistry of basalts and mantle inclusions from the Lunar Crater Volcanic  
795 Field, Nevada; petrogenetic and geodynamic implications. M.Sc. Thesis, The Ohio State University.

796

797 Kumar, P., Yuan, X., Kind, R., and Mechie, J., (2012) The lithosphere-asthenosphere boundary  
798 observed with USArray receiver functions. *Solid Earth*, 3, 149-159.

799

800 Leake, B.E., Woolley, A.R., Arps, C.E.S., Birch, W.D., Gilbert, M.C., Grice, J.D., Hawthorne, F.C.,  
801 Kato, A., Kisch, H.J., Krivovichev, V.G., Linthout, K., Laird, J., Mandarino, J.A., Maresch, W.V.,  
802 Nickel, E.H., Rock, N.M.S., Schumacher, J.C., Smith, D.C., Stephenson, N.C.N., Ungaretti, L.,  
803 Whittaker, E.J.W., and Guo, Y.Z., (1997) Nomenclature of amphiboles: report of the subcommittee on  
804 amphiboles of the international mineralogical association, commission on new minerals and mineral  
805 names. *American Mineralogist*, 82, 1019–1037

806

807 Lee, C.A., Luffi, P., Plank, T., Dalton, H., and Leeman, W.P. (2009) Constraints on the depths and  
808 temperatures of basaltic magma generation on Earth and other terrestrial planets using new  
809 thermobarometers for mafic magmas. *Earth and Planetary Science Letters*, 279, 20-33.

810

811 Le Maitre R.W., Streckeisen, A., Zanettin, B., Le Bas, M.J., Bonin, B., Bateman, P., Bellieni, G.,  
812 Dudek, A., Efremova, S., Keller, J., Lamere, J., Sabine, P.A., Schmid, R., Sorensen, H., and Woolley,  
813 A.R., (2002) *Igneous Rocks: A Classification and Glossary of Terms, Recommendations of the*  
814 *International Union of Geological Sciences, Subcommission of the Systematics of Igneous Rocks*. 256  
815 p. Cambridge University Press.

816

817 Loucks, R. (1996) A precise Olivine-Augite Mg-Fe-exchange geothermometer. *Contributions to*

818 Mineralogy and Petrology, 125, 140-150.

819

820 Luhr, J.F., and Simkin, T., (1993) Parícutín: The Volcano Born in a Mexican Cornfield. 441 p.

821 Geoscience Press, Inc., Phoenix, Arizona.

822

823 Luhr, J.F., Aranda-Gómez, J.J., and Housh, T.B., (1995) San Quintín volcanic field, Baja California

824 Norte, México: Geology, petrology, and geochemistry. Journal of Geophysical Research, 100, 10353-

825 10380.

826

827 Lum, C.C.L., (1986) Aspects of petrogenesis of alkali basalts from the Lunar Crater Volcanic Field,

828 Nevada. M.S. thesis, Ohio State University, Columbus, Ohio.

829

830 Lum, C.C.L., and Leeman, W.P., (1989) Isotopic variation in continental basaltic lavas as indicators of

831 mantle heterogeneity: Examples from the Western U.S. Cordillera. Journal of Geophysical Research,

832 94, B6, 7871-7884.

833 Maaløe, S., (2011) Olivine phenocrysts growth in Hawaiian tholeiites: evidence for supercooling.

834 Journal of Petrology, 7-8, 1579-1589

835

836 Marsh, B.D., (1988) Crystal size distribution (CSD) in rocks and the kinetics and dynamics of

837 crystallization I. Theory: Contributions to Mineralogy and Petrology, 99, 277–291.

838

839 Marsh, B.D., (1998) On the interpretation of crystal size distributions in magmatic systems: Journal of

840 Petrology, 39, 553–600.

841 McGee, L.E., Smith, I.E.M., Millet, M.-A., Handley, H.K., and Lindsay, J.M., (2013) Asthenospheric  
842 control on melting processes in a monogenetic basaltic system: a case study of the Auckland Volcanic  
843 Field, New Zealand. *Journal of Petrology*, doi:10.1093/petrology/egt043.

844

845 Mayer, B., Jung, S., Romer, R.L., Pfänder, J.A., Klügel, A., Pack, A., Gröner, E., (2014). Amphibole in  
846 alkaline basalts from intraplate settings: implications for the petrogenesis of alkaline lavas from the  
847 metasomatized lithospheric mantle. *Contributions to Mineralogy and Petrology*, 167:989, doi:  
848 10.1007/s00410-014-0989-3

849 Menzies, M.A., (1989) Cratonic, circumcratonic, and oceanic mantle domains beneath the Western  
850 United States. *Journal of Geophysical Research*, 94(B6), 7899-7915, doi: 10.06.1989

851

852 Mock, A., and Jerram, D.A., (2005) Crystal Size Distributions (CSD) in three dimensions: Insights  
853 from the 3D reconstruction of a highly porphyritic rhyolite. *Journal of Petrology*, 46,1525-1541.

854

855 Morgan, D. J. and Jerram, D. A., (2006) On estimating crystal shape for crystal size distribution  
856 analysis. *Journal of Volcanology and Geothermal Research*, 154, 1-7.

857

858 Morimoto, N., (1989) Nomenclature of Pyroxenes. *Canadian Mineralogist*, 27, 143-156

859

860 Muffler, L.J.P., Clynne, M.A., Calvert, A.T., and Champion, D.E., (2011) Diverse, discrete, mantle-  
861 derived batches of basalt erupted along a short normal fault zone: the Poison Lake chain, southernmost  
862 Cascades. *Geological Society of America Bulletin*, 123, 2177-2200.

863

864 Naumann, T.R., Smith, E.I., Shafiqullah, M., Damon, P.E., (1991) New ages for Pliocene mafic to

865 intermediate volcanic rocks in the Reville Range, Nevada. *Isochron/West*, 57, 12-16.

866

867 Nicholis, M.G., and Rutherford, M.J., (2004) Experimental constraints on magma ascent rate for the

868 Crater Flat volcanic zone hawaiite. *Geology*, 32, 489-492.

869

870 Nimis, P. and Ulmer, P. (1998) Clinopyroxene geobarometry of magmatic rocks. Part 1: An expanded

871 structural geobarometer for anhydrous and hydrous, basic and ultrabasic systems. *Contributions to*

872 *Mineralogy and Petrology*, 133, 122-135.

873

874 Nimis, P., (1999) Clinopyroxene geobarometry of magmatic rocks. Part 2. Structural geobarometers for

875 basic to acid, tholeiitic and mildly alkaline magmatic systems. *Contributions to Mineralogy and*

876 *Petrology*, 135, 62-74.

877

878 Papike, J.J., Cameron, K.L., Baldwin, K. (1974) Amphiboles and pyroxenes: Characterization of

879 OTHER than quadrilateral components and estimates of ferric iron from microprobe data. *Geological*

880 *Society of America, Abstracts with Programs*, 6, 1053-1054.

881

882 Petermann. M., and Hirschmann, M.M., (2003) Partial melting experiments on a MORB-like

883 pyroxenite between 2 and 3 GPa: Constraints on the presence of pyroxenite in basalt source regions

884 from solidus location and melting rate. *Journal of Geophysical Research*, 108(B2,2125), doi:

885 10.1029/2000JB000118.

886

887 Pioli, L., Erlund, E., Johnson, E., Cashman, K., Wallace, P., Rosi, M., and Delgado-Granados, H.,

888 (2008) Explosive dynamics of violent Strombolian eruptions: The eruption of Parícutín Volcano 1943-

889 1952 (México). *Earth and Planetary Science Letters*, 271, 359-368.

890

891 Powell, M., and Powell, R., (1974) An olivine-clinopyroxene geothermometer. Contributions to  
892 Mineralogy and Petrology, 48, 249-263.

893

894 Putirka, K., (2008) Thermometers and barometers for volcanic systems. Reviews in Mineralogy and  
895 Geochemistry, 69, 61-120

896

897 Putirka, K., Jean, M., Cousens, B., Sharma, Rl, Torrez, G, and Carlson, C., (2012) Cenozoic volcanism  
898 in the Sierra Nevada and Walker Lane, California, and a new model for lithospheric degradation.  
899 Geosphere, 8, 265-291, doi: 10.1130/GES00728.1.

900

901 Ridolfi, F., Renzulli, A., and Puerini, M., (2010) Stability and chemical equilibrium of amphibole in  
902 calc-alkaline magmas: an overview, new thermobarometric formulations and application to subduction-  
903 related volcanoes. Contributions to Mineralogy and Petrology, 160, 45–66, doi:10.1007/s00410-009-  
904 0465-7

905

906 Ridolfi, F., and Renzulli, A., (2012) Calcic amphiboles in calc-alkaline and alkaline magmas:  
907 thermobarometric and chemometric empirical equations valid up to 1,130°C and 2.2 GPa.  
908 Contributions to Mineralogy and Petrology, 163, 877-895.

909

910 Rowe, M.C., Peate, D.W., and Peate, I.U., (2011) An investigation into the nature of the magmatic  
911 plumbing system at Parícutin Volcano, Mexico. Journal of Petrology, 52, 2187-2220

912

913 Scott, D., and Trask, N.J., (1971) Geology of the Lunar Crater Volcanic Field, Nye County, Nevada.

914 USGS Professional Paper 599-I, 11-22.

915

916 Shepard, M. K., Arvidson, R. E., Caffee, M., Finkel, R., and Harris, L., (1995) Cosmogenic exposure  
917 ages of basalt flows; Lunar Crater volcanic field, Nevada. *Geology*, 23, 21-24.

918

919 Simakin, A., Zakrevskaya, O., and Salova, T., (2012a) Novel amphibole geo-barometer with  
920 application to mafic xenoliths. *Earth Science Research*, 1, doi: 10.5539/esr.v1n2p82

921

922 Simakin, A.G., Salova, T.P., Bondarenko, G.V., (2012b) Experimental study of magmatic melt  
923 oxidation by CO<sub>2</sub>. *Petrology*, 20(7), 593-606.

924

925 Smith, R.L., and Luedke, R.G., (1984) Potentially active volcanic lineaments and loci in the western  
926 conterminous United States. In *Explosive volcanism: Inception, evolution, and hazards: Studies in*  
927 *Geophysics*, National Academy Press, Washington DC, p. 47-66.

928

929 Smith, I.E.M., Blake, S., Wilson, C.J.N., and Houghton, B.F., (2008) Deep-seated fractionation during  
930 the rise of a small-volume basalt magma batch: Crater Hill, Auckland, New Zealand. *Contributions to*  
931 *Mineralogy and Petrology*, 155, 511-527.

932

933 Smith, D., (2000) Insights into the evolution of the uppermost continental mantle from xenolith  
934 localities on and near the Colorado Plateau and regional comparisons. *Journal of Geophysical*  
935 *Research*, 105, 16769-16781

936

937 Sobolev, A.V., Hoffmann, A.W., Kuzmin, D.V., Yaxley, G.M., Arnt, N.T., Chung, S., Danyushevsky,  
938 L. V., Elliott, T., Frey, F.A., Garcia, M.O., Gurenko, A.A., Kamenetsky, V.S., Kerr, A.C.,

939 Krivolutskaya, N.A., Matvienkov, V.V., Nikogozian, I.K., Rocholl, A., Sigurdsson, I.A.,  
 940 Sushchevskaya, N. M., Teklay, M., (2007) The amount of recycled crust in sources of mantle-derived  
 941 melts. *Science* 316, 412-417.

942

943 Stickney, E.K., (2004) The volcanology and petrogenesis of the northern Lunar Crater Volcanic Field,  
 944 Nye County, Nevada. M.Sc. Thesis. University of Nevada, Las Vegas.

945

946 Sun, S.S., and McDonough, W.F., (1989) Chemical and isotopic systematics of oceanic basalts:  
 947 implications for mantle composition and processes. *Geological Society of London, Special*  
 948 *Publications*, 42, 313-345.

949

950 Thirwall, M.F., Upton, B.G.J., and Jenkins, C. (1994) Interaction between continental lithosphere and  
 951 the Iceland plume-Sr-Nd-Pb isotope geochemistry of Tertiary basalt, NE Greenland. *Journal of*  
 952 *Petrology*, 35, 839-879.

953

954 Tuff, J., Takahashi, E., and Gibson, S.A., (2005) Experimental constraints on the role of garnet  
 955 pyroxenite in the genesis of high-Fe mantle plume derived melts. *Journal of Petrology*, 46, 2023-2058.

956

957 Valentine, G.A., and Cortés, J.A., (2013) Time and space variations in magmatic and phreatomagmatic  
 958 eruptive processes at Easy Chair (Lunar Crater Volcanic Field, Nevada, USA). *Bulletin of*  
 959 *Volcanology*, 75, doi:10.1007/s00445-013-0752-z.

960

961 Valentine, G.A., and Gregg, T.K.P., (2008) Continental basaltic volcanoes — Processes and problems.  
 962 [Journal of Volcanology and Geothermal Research](#), 177, 857-873.

963

964 Valentine, G.A., and Hirano, H., (2010) Mechanisms of low-flux intraplate volcanic fields – Basin and  
 965 Range (North America) and northwest Pacific Ocean. *Geology*, 38, 55-58.

966

967 Valentine, G.A., and Keating, G.N., (2007) Eruptive styles and inferences about plumbing systems at  
 968 Hidden Cone and Little Black Peak scoria cone volcanoes (Nevada, U.S.A.) *Bulletin of Volcanology*,  
 969 70, 105-113.

970

971 Valentine, G.A., and Perry, F.V., (2006) Decreasing magmatic footprints of individual volcanoes in a  
 972 waning basaltic field. *Geophysical Research Letters*, 33, L14305.

973

974 Valentine, G.A., and Perry, F.V., (2007) Tectonically controlled, time-predictable basaltic volcanism  
 975 from a lithospheric mantle source (central Basin and Range Province, USA). *Earth and Planetary*  
 976 *Science Letters*, 261, 201-216.

977

978 Valentine, G.A., Shufelt, N.L., and Hintz, A.R.L., (2011) Models of maar volcanoes, Lunar Crater  
 979 (Nevada, USA). *Bulletin of Volcanology*, 73, 753-765.

980

981 Vaniman, D.T., Crowe, B.M., and Gladney, E.S., (1982) Petrology and geochemistry of hawaiiite lavas  
 982 from Crater Flat, Nevada. *Contributions to Mineralogy and Petrology*, 80, 341-357.

983



984 Wade, J., Wood, B.J., (2005) Core formation and the oxidation state of the Earth. Earth and Planetary  
985 Science Letters, 236, 78-95.

986

987 Wang, K, Plank, T., Walker, J.D., Smith, E.I., (2001) A mantle melting profile across the Basin and  
988 Range, SW USA. Journal of Geophysical Research, 107(B1), doi: 10.1029/2001JB000209.

989

990 White, J.D.L., and Ross, P.-S., (2011) Maar-diatreme volcanoes: a review. Journal of Volcanology  
991 and Geothermal Research, 201, 1-29.

992

993 Yogodzinski, G. M., Naumann, T.R., Smith, E.I., Bradshaw, T.K., and Walker, J.D., (1996) Evolution  
994 of a mafic volcanic field in the central Great Basin, south central Nevada. Journal of Geophysical  
995 Research, 101(B8), 17425-17445.

996

997 **Figure Captions**

998

999 Figure 1: Location of the Lunar Crater Volcanic Field in the western U.S.A. and the State of Nevada  
1000 showing the Pancake and Reville Range within the volcanic field. Dashed lines are the main roads in  
1001 the area. Red box encompasses the study area (see Figure 2).

1002

1003 Figure 2: Simplified geological map of the northern part of the Lunar Crater Volcanic Field,  
1004 highlighting the four volcanoes studied in this work. Outline of tephra deposits from Johnson (2013).

1005

1006 Figure 3: Total Alkali versus silica diagram according to Le Maitre et al. (2002). Hi Desert basalt  
1007 (Qhib) open circle, Mizpah basalt (Qmzb) open square, Giggie Spring basalt (Qgsb) asterisk, Marcath  
1008 volcano products (Qm) crosses. All whole-rock figures plotted using PINGU (Cortés and Palma, 2011).

1009

1010 Figure 4: Whole-rock major element variation diagrams versus MgO for the samples of this study.  
1011 Symbols as in Figure 3.

1012

1013 Figure 5: Rare Earth Element diagram normalized according to Sun and McDonough (1989). Symbols  
1014 as in Figure 3.

1015

1016 Figure 6: Spider diagrams normalized according to OIB from Sun and McDonough (1989). Symbols as  
1017 in Figure 3.

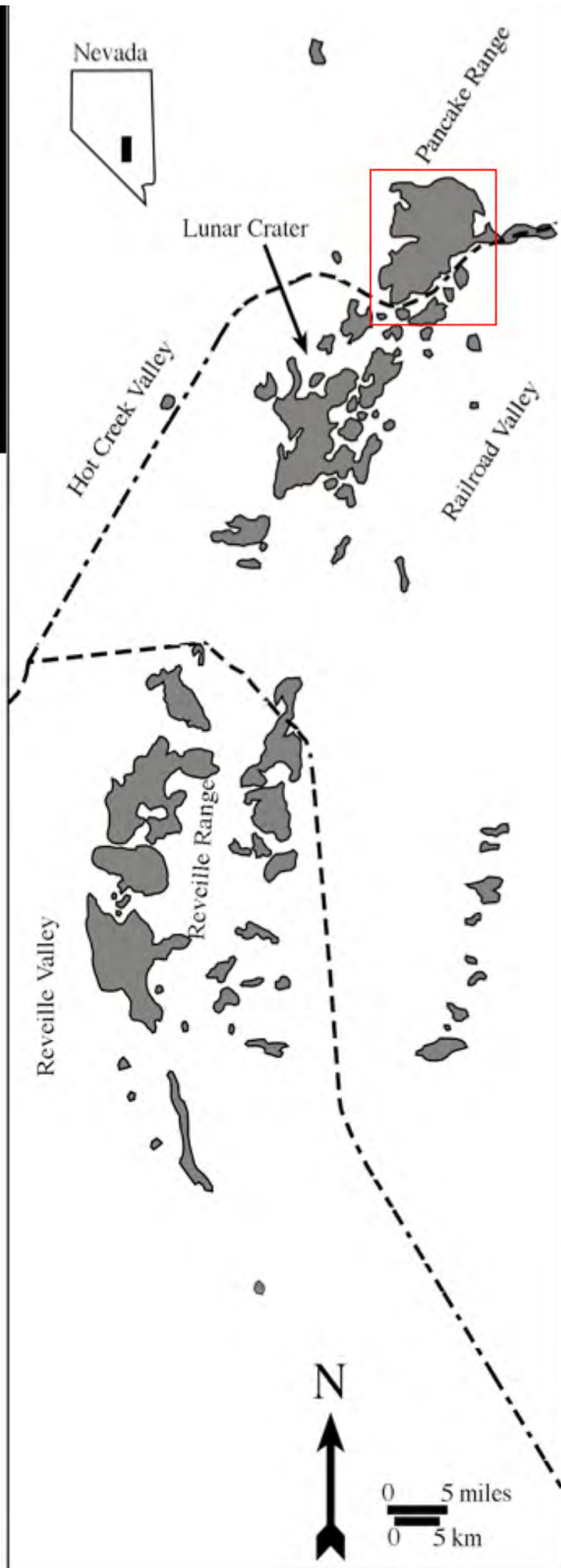
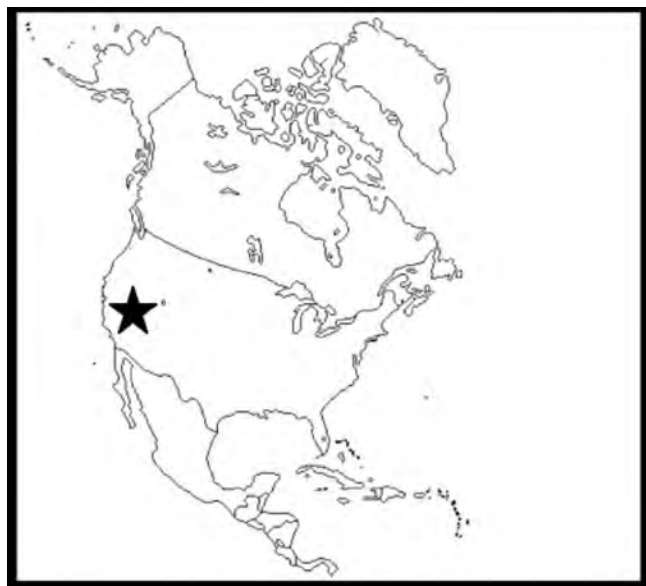
1018

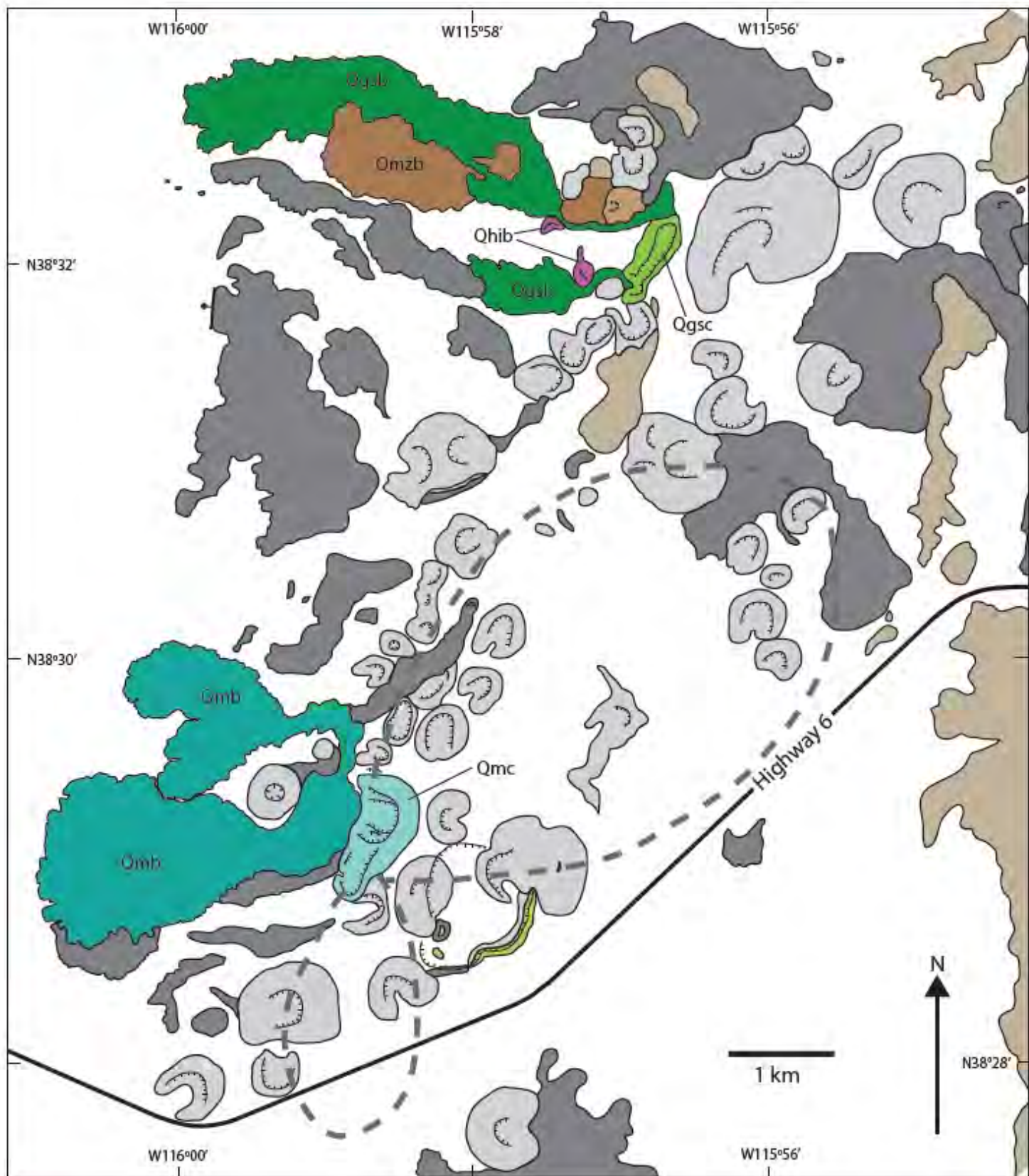
1019 Figure 7: a) La/Yb vs. Zr/Nb b) Rb/Zr vs. Ni/Zr c) La/Yb vs. Dy/Yb. Symbols as in Figure 3.

1020

1021 Figure 8: a) La/Nb vs Nb [ppm] b) Nb/Ta vs Nb [ppm]. Fields as defined in Barth et al., (2000).  
 1022 Symbols as in Figure 3.  
 1023  
 1024 Figure 9: Mineral classification based on mineral chemistry for a) olivine (Deer et al., 1996) b)  
 1025 pyroxenes (Morimoto, 1989) c) plagioclase (Deer et al., 1996) and d) amphiboles (Leake, 1997) from  
 1026 electron microprobe analyses in the studied samples. Symbols of the units as in Figure 3.  
 1027  
 1028 Figure 10: (a)  $\text{Fe}^{2+}/\text{Mn}$  vs.  $\% \text{Fo} = \text{Mg}/(\text{Mg} + \text{Fe}^{2+} + \text{Mn})$  and (b)  $100 \times \text{Mn}/\text{Fe}^{2+}$  vs.  $100 \times \text{Ca}/\text{Fe}^{2+}$  ( $\% \text{Fo} > 85$ )  
 1029 in mineral chemistry analyses of olivine recalculated as cation per formula unit from electron  
 1030 microprobe analyses. Symbols of the units as in Figure 3.  
 1031  
 1032 Figure 11. Natural logarithm of the density population ( $\text{mm}^{-4}$ ) vs. size (mm) plots of the crystal size  
 1033 distribution for a) olivine b) clinopyroxene c) plagioclase and d) spinel in the studied samples.  
 1034 Minimum crystal sizes that can be measured using ImageJ in an SEM image are ~10-20 pixels long,  
 1035 equivalent to ~5% of the average scale bar of ~300 pixels (around ~0.01-0.02 mm in most of our  
 1036 images except images for measuring oxides with minimum sizes of 0.001-0.002 mm). Black asterisk:  
 1037 Giggle Spring basalt (Qgsb) sampled at the vent. Light grey asterisk: Giggle Spring basalt (Qgsb) lava.  
 1038 Black open squares: Mizpah basalt (Qmzb), Black crosses: Marcath volcano products (Qm).  
 1039  
 1040 Figure 12: La/Yb vs. Dy/Yb plots with different models of partial melting of a mantle source. Data  
 1041 points are normalized with C1 chondrite (Sun and McDonough 1989), symbols as in Figure 3. (a)  
 1042 Partial melting of lherzolite source: grey line and filled triangles is a model of batch melting of a garnet  
 1043 lherzolite with 11.5 % of garnet; black line with filled circles is a model of batch melting of a garnet  
 1044 lherzolite with 6% of garnet, black line with open squares is a model of batch melting of a garnet  
 1045 lherzolite with 2% of garnet, black line with open triangles is a model of batch melting of a spinel

1046 lherzolite. Tick marks on all curves are at 5% melting intervals. (b) Partial melting of pyroxenite  
1047 source: black line and filled triangles is a model of batch melting of a garnet pyroxenite with 11%  
1048 garnet; black line with filled circles is a model of batch melting of a garnet pyroxenite with 9% garnet,  
1049 black line with open squares models batch melting of a garnet pyroxenite with 5% garnet. Tick marks  
1050 on all curves are at 5% melting intervals.





#### Studied units

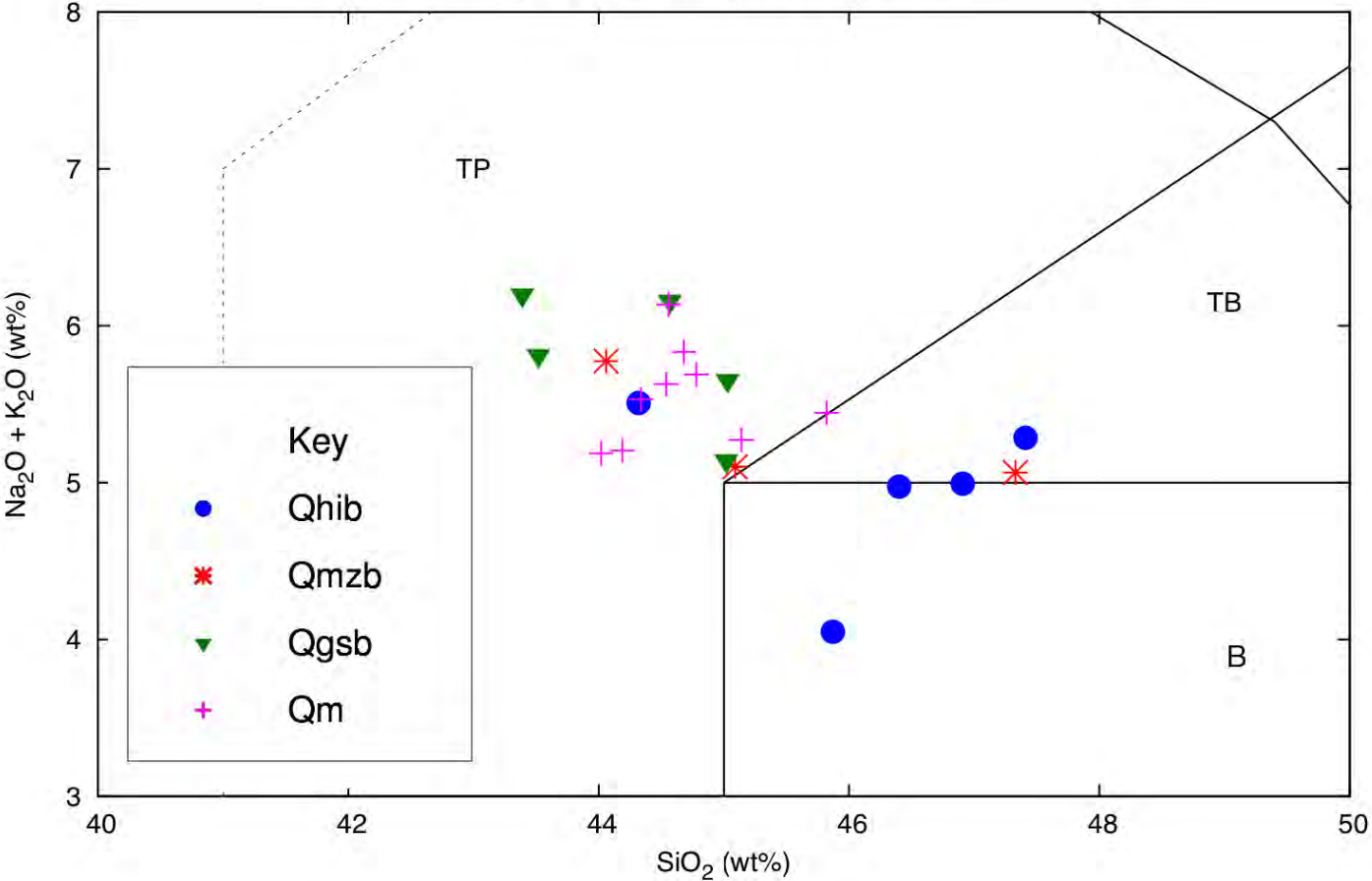
Qmzc	Marcath basalt (38 ± 10 ka)
Qmzb	Qmb - lava; Qmzc - pyroclastic cone
Qgsc	Giggle Spring basalt (< 80 ka)
Qgslb	Qgsb - lava; Qgsc - pyroclastic cone
Qhib	Hi Desert basalt (two agglomerate cones)
Qmzc	Mizpah basalt (620-740 ka)
Qmzb	Qmzb - lava; Qmzc - pyroclastic cone

#### Other units

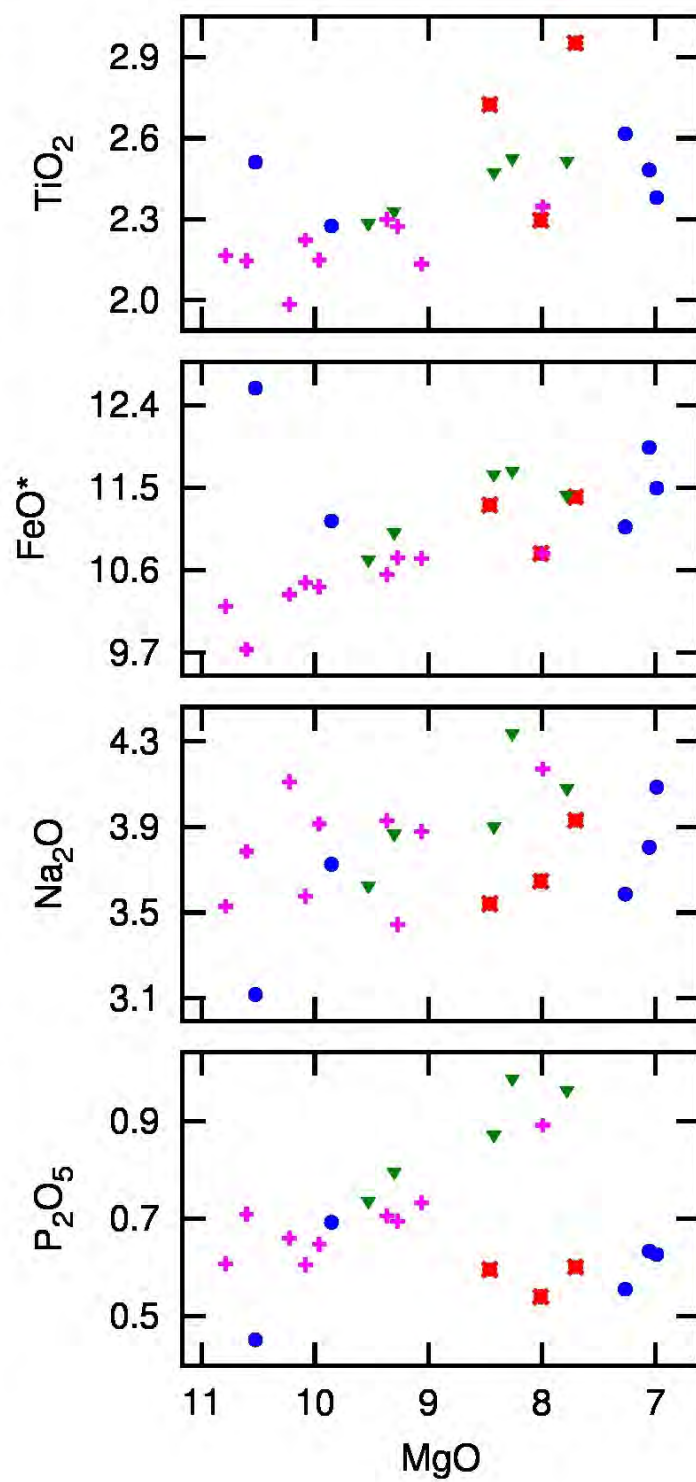
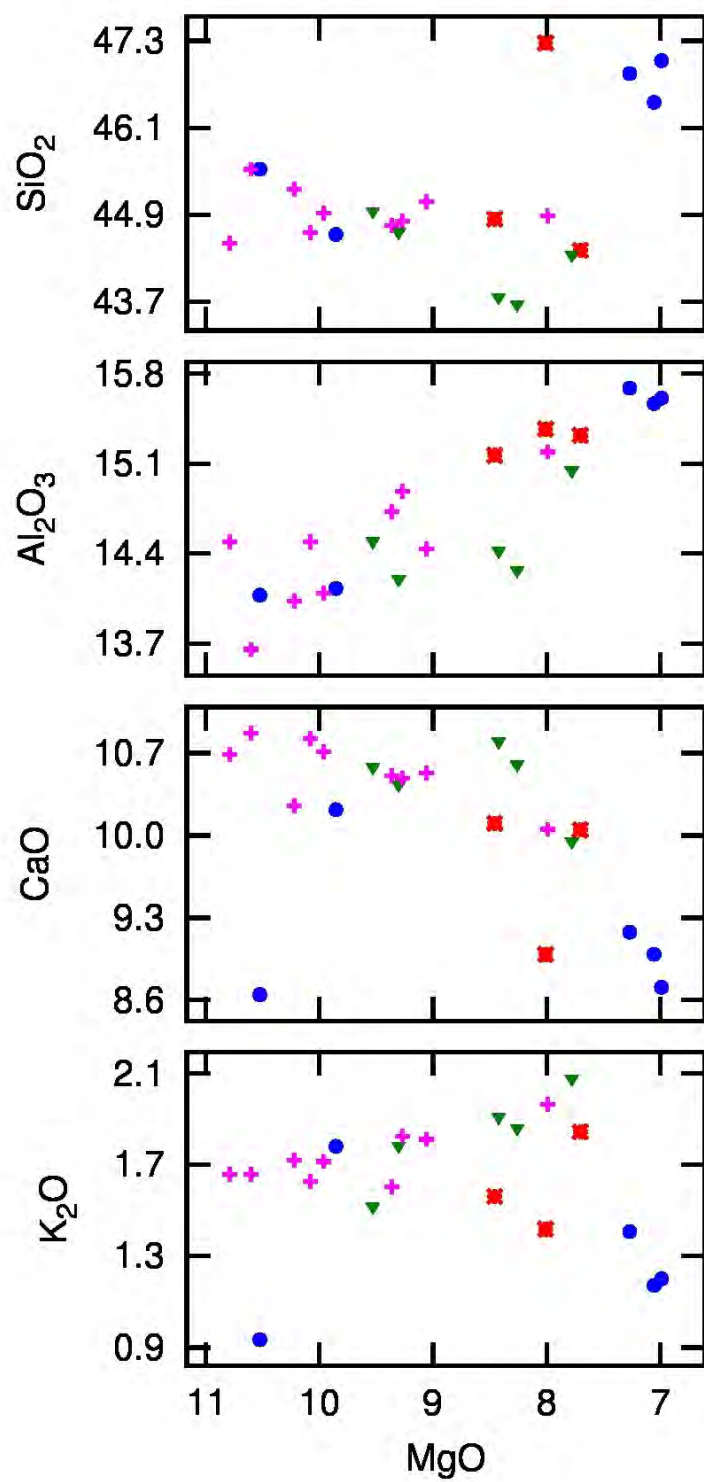
	Quaternary alluvium, colluvium, and eolian deposits (locally includes tephra)
	Quaternary basalt (undifferentiated). Lavas dark grey, pyroclastic cones light grey
	Quaternary lapilli tuff and tuff breccia
	Oligocene-Miocene silicic volcanic rocks

	Approximate outer limits of continuous tephra (Marcath)
	Crater rim
	Normal fault (bar on hanging wall)

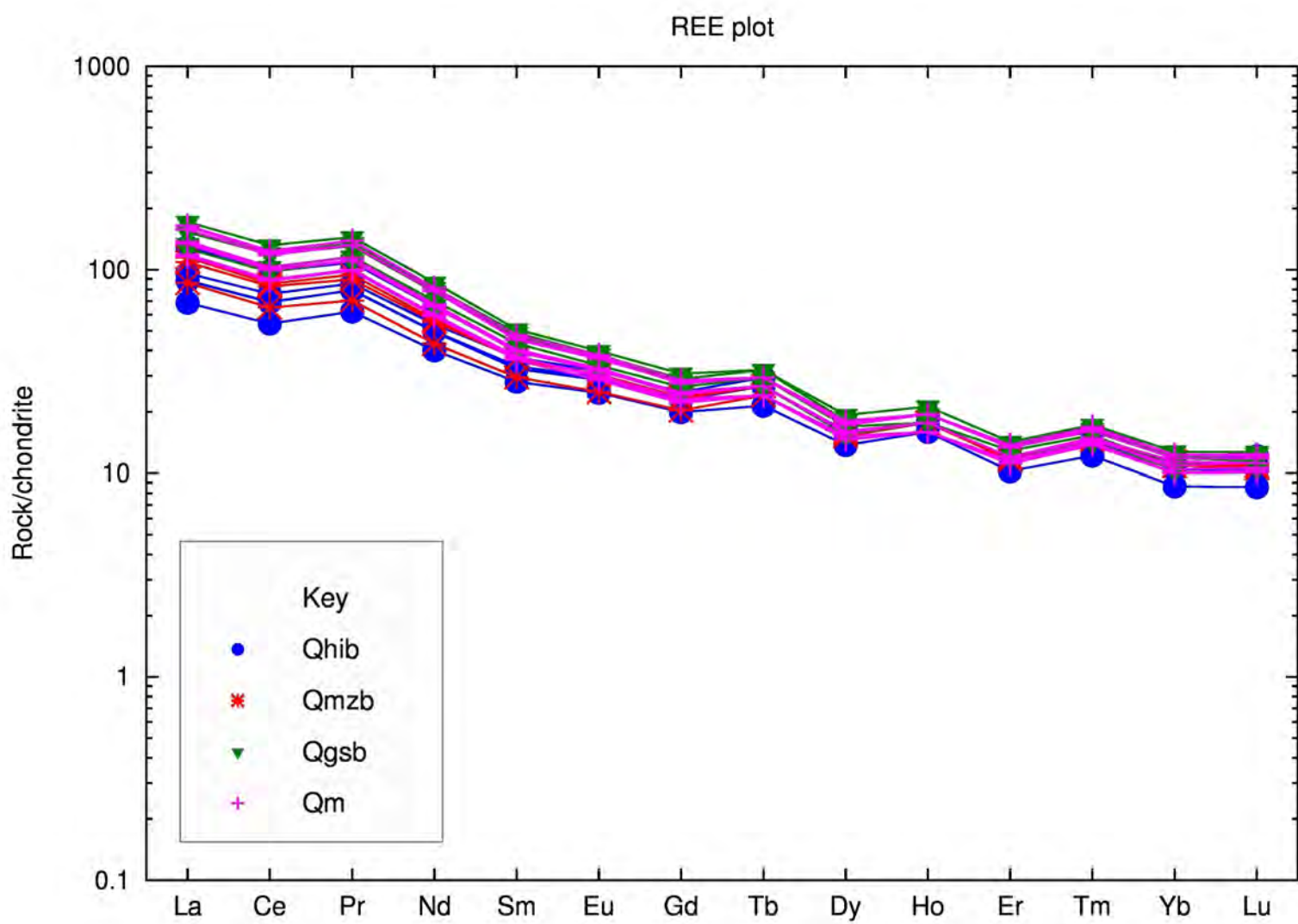
TAS Diagram (Le Maitre et al., 1989)



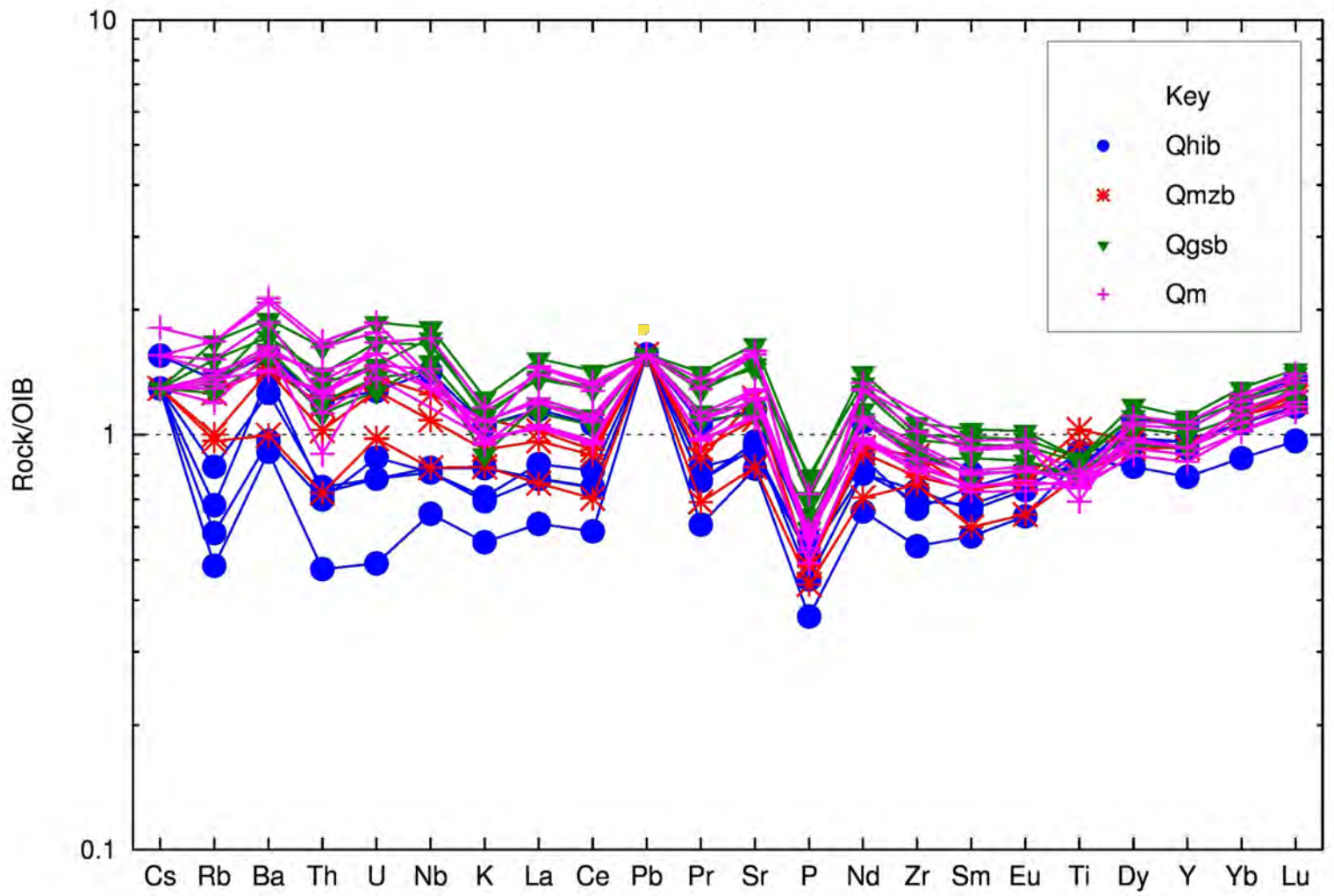


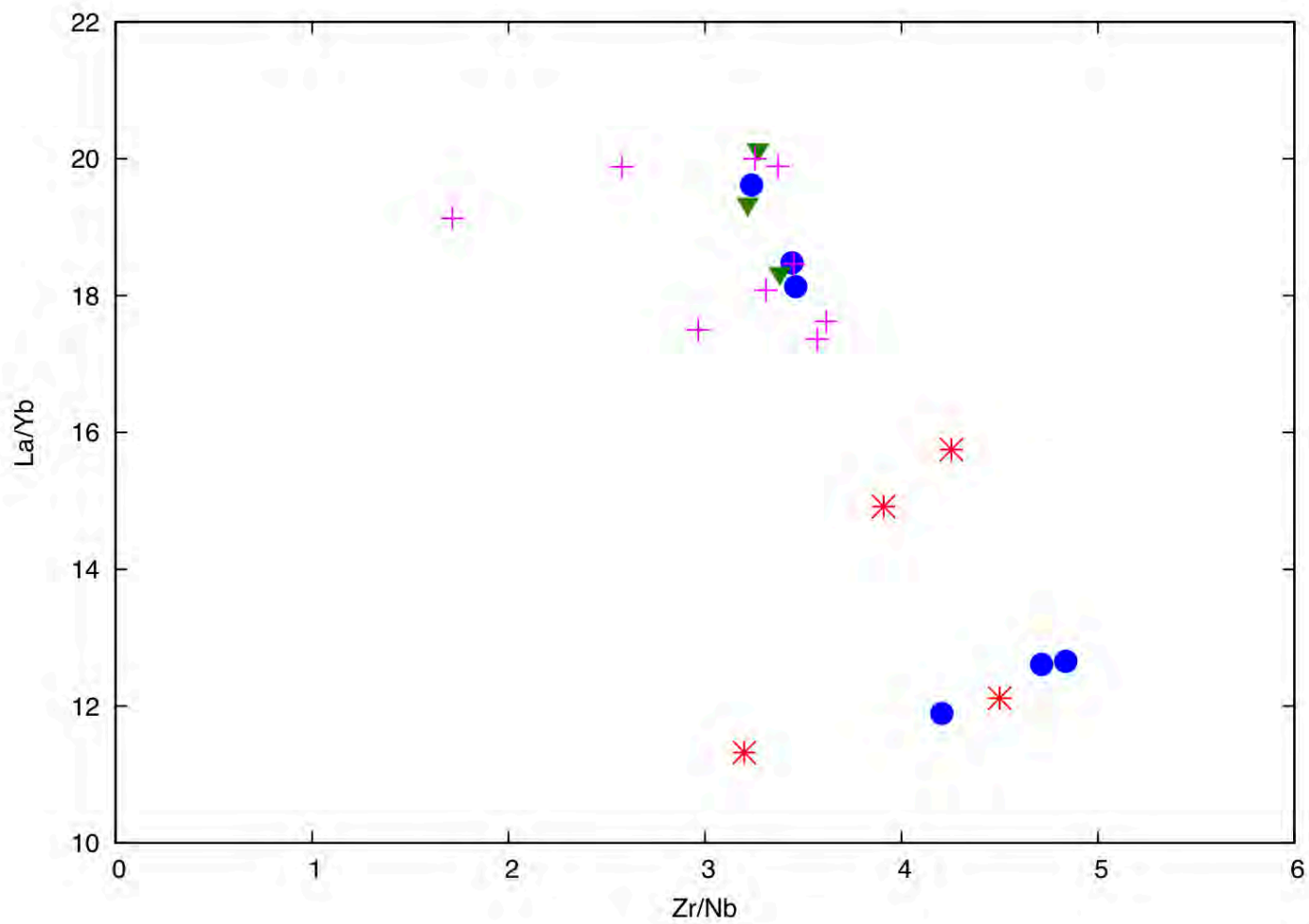


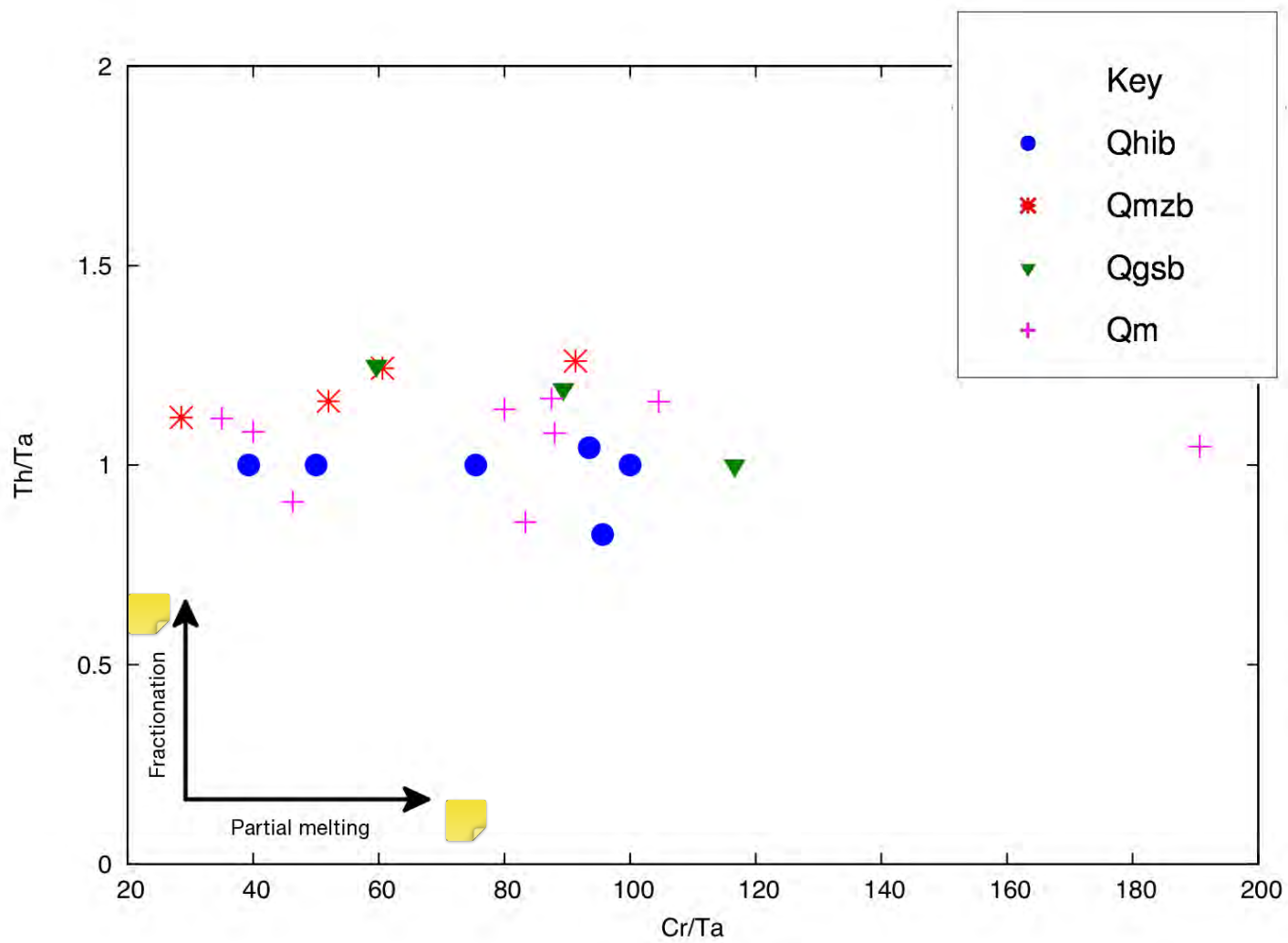


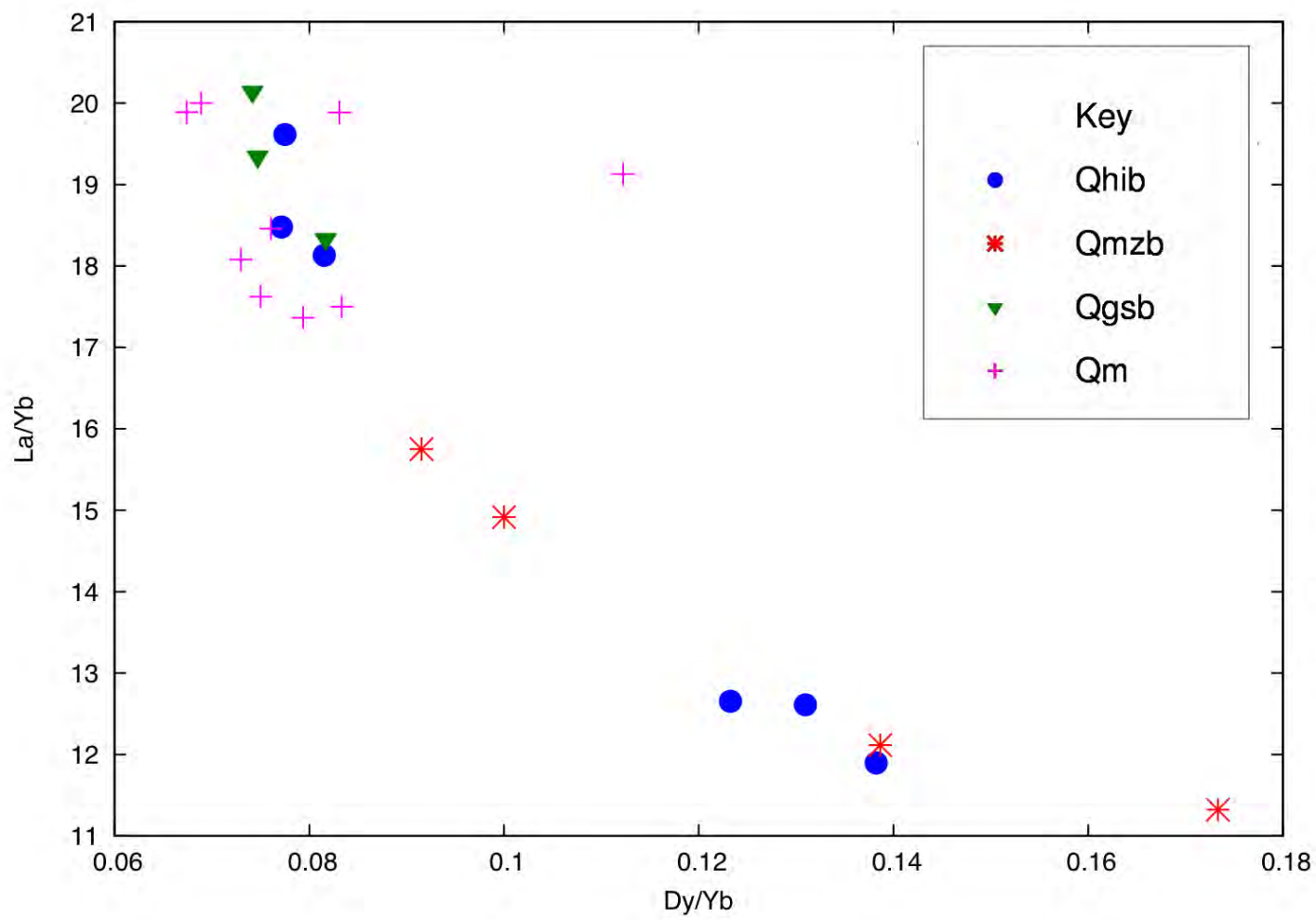


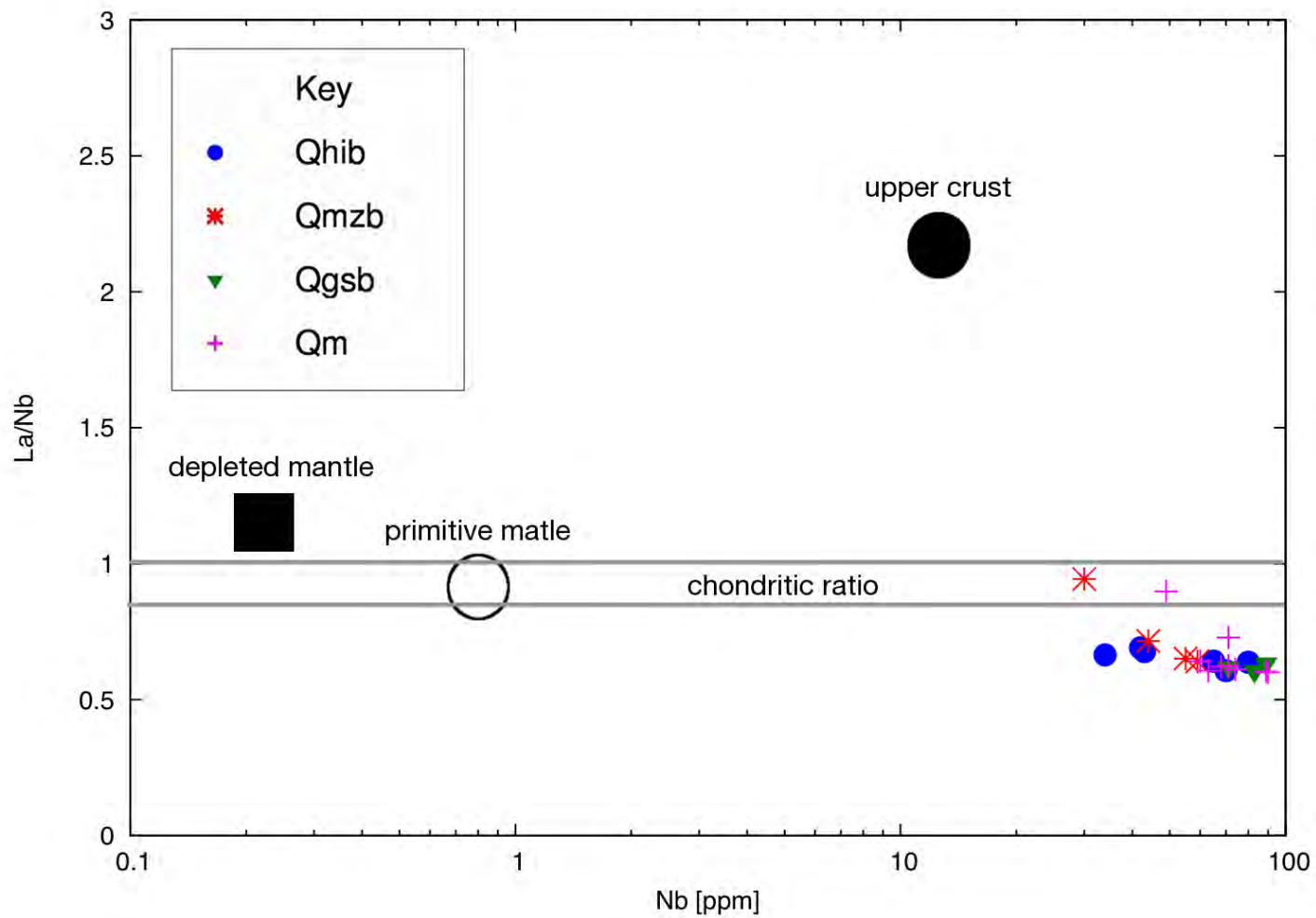
Spider Diagram

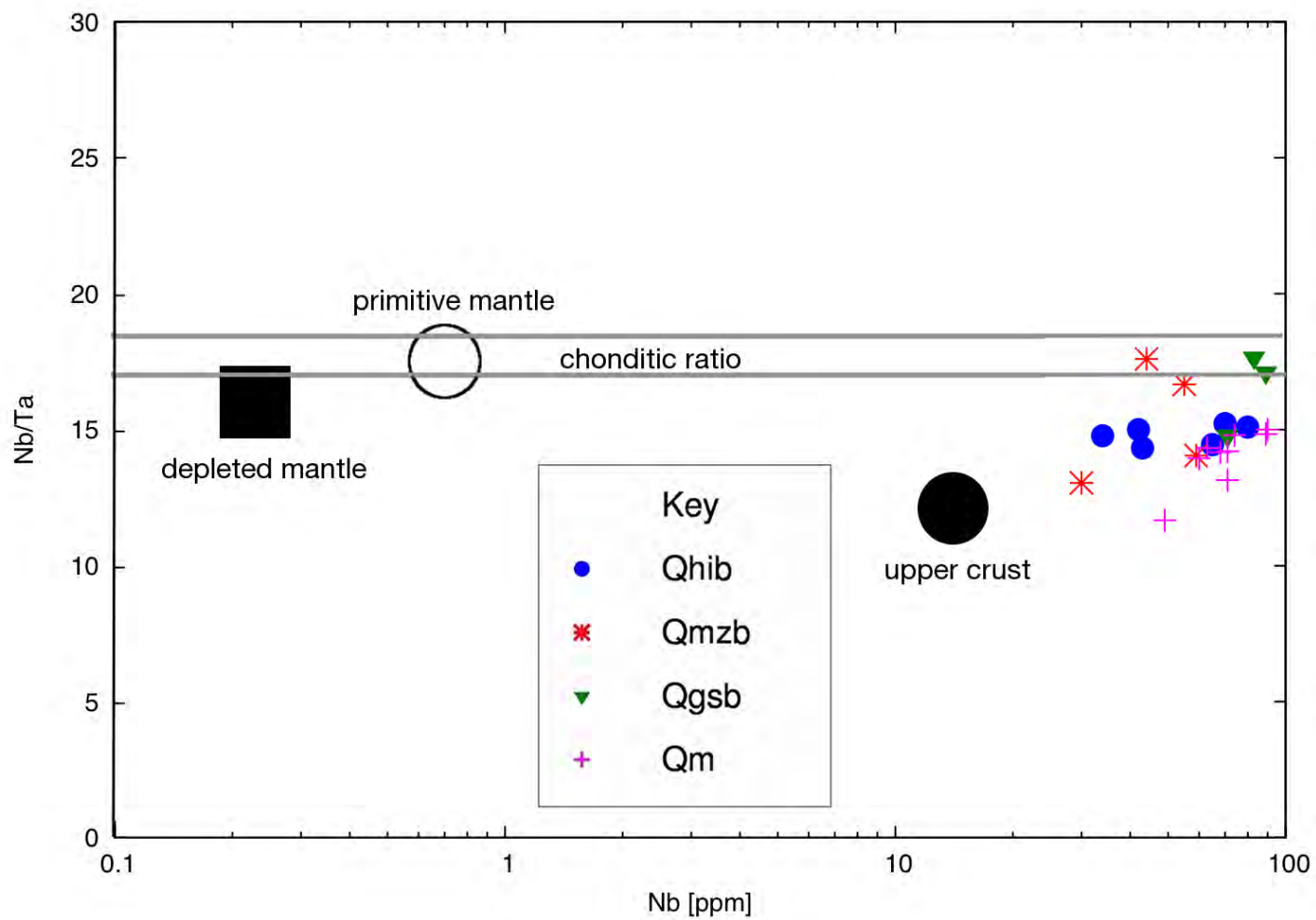


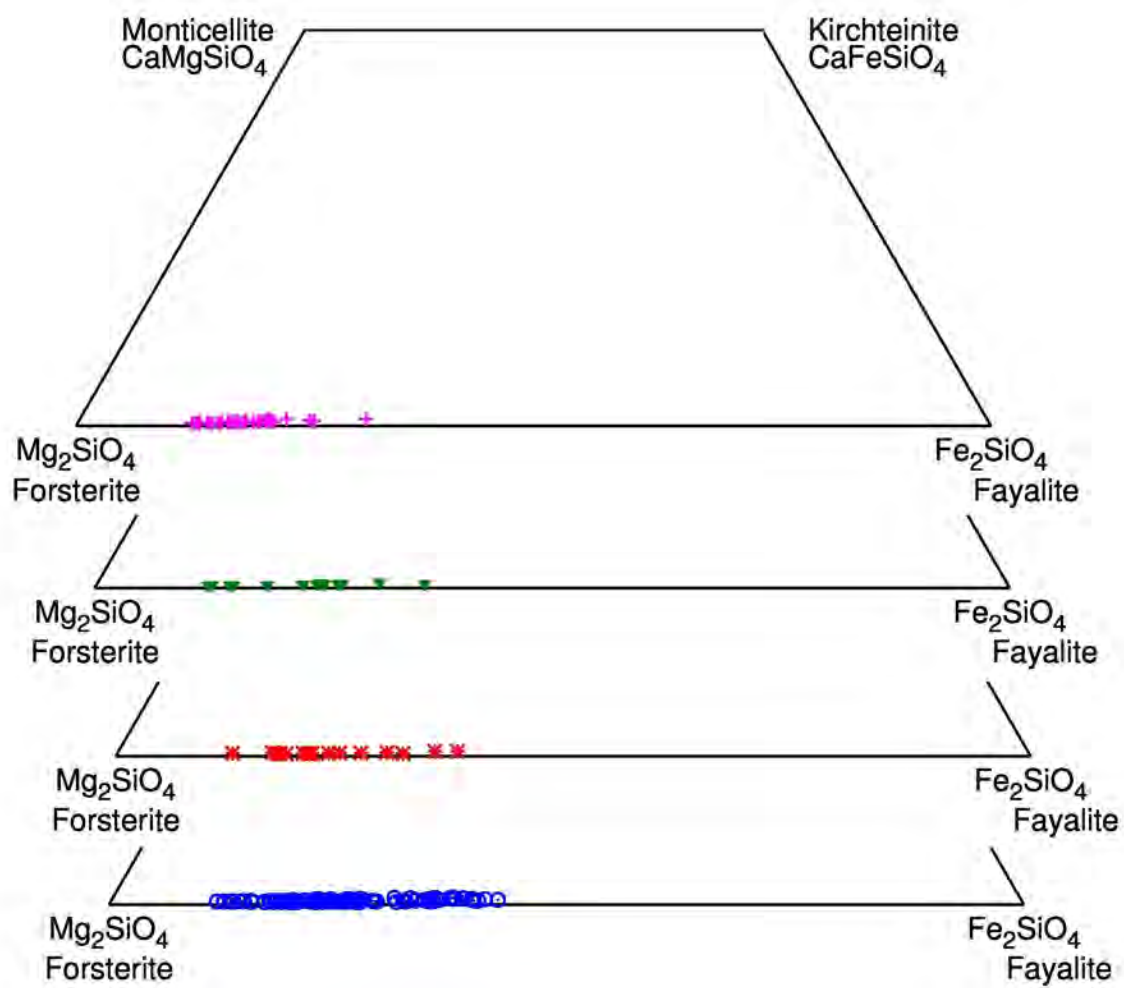




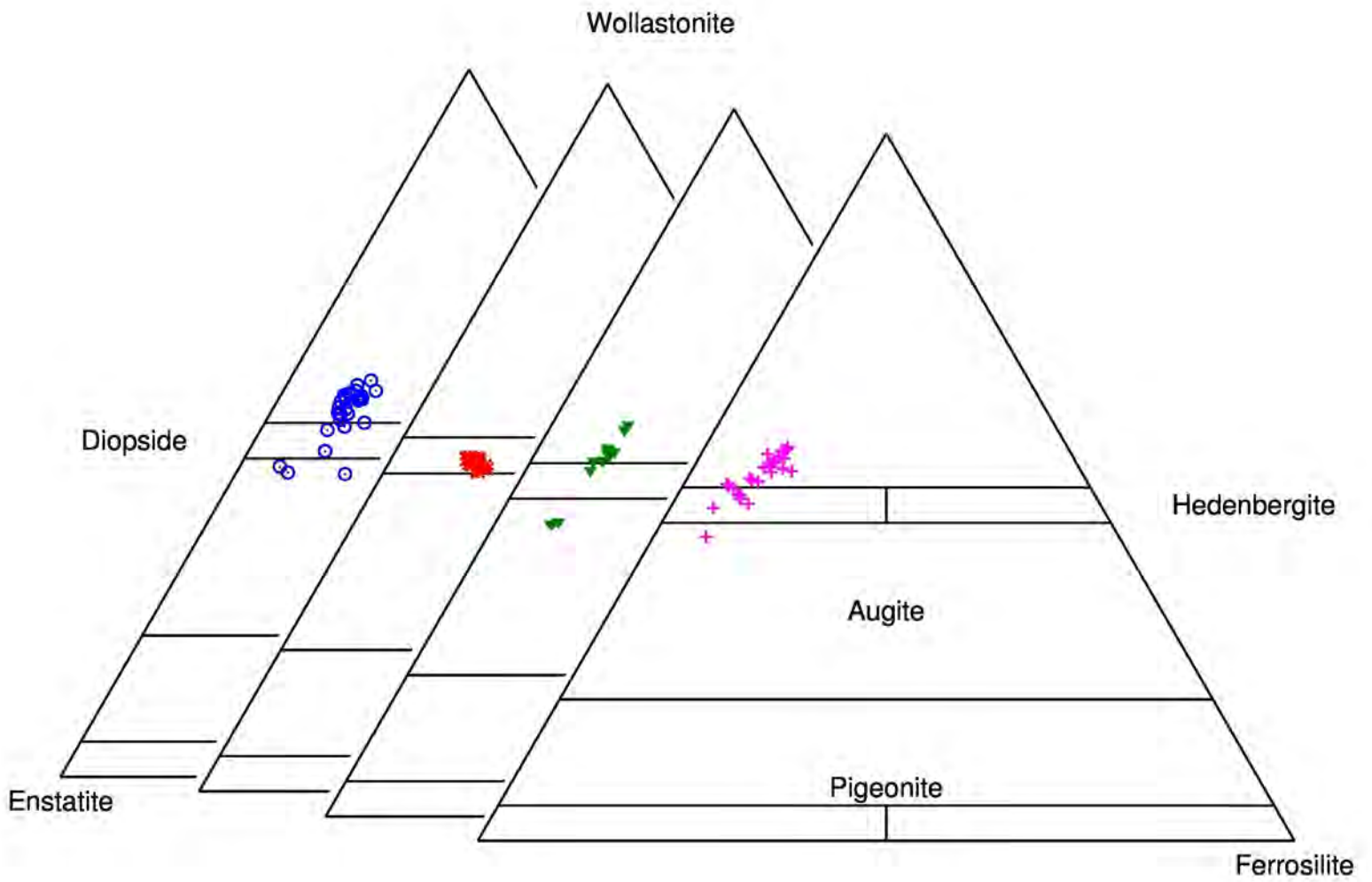


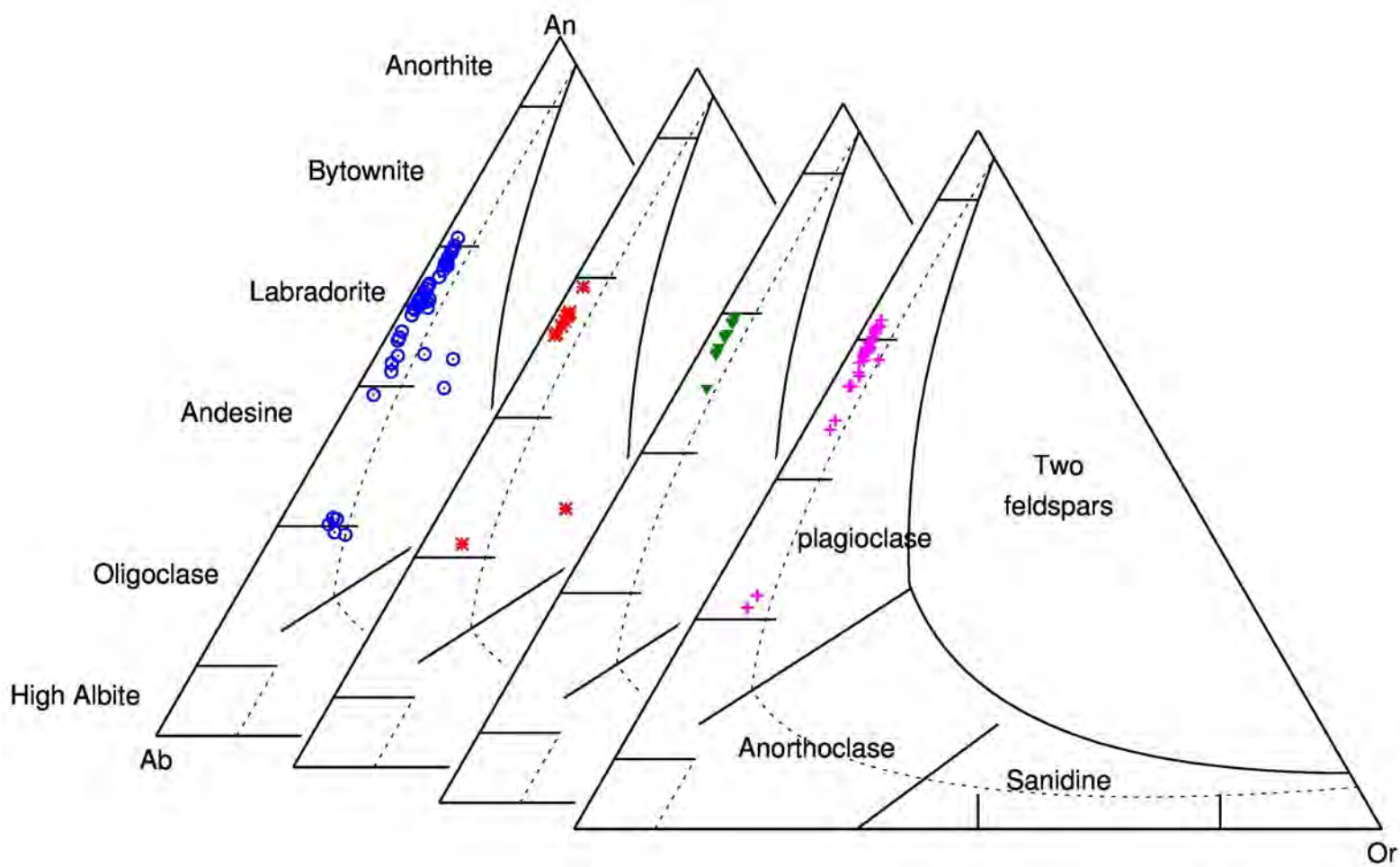


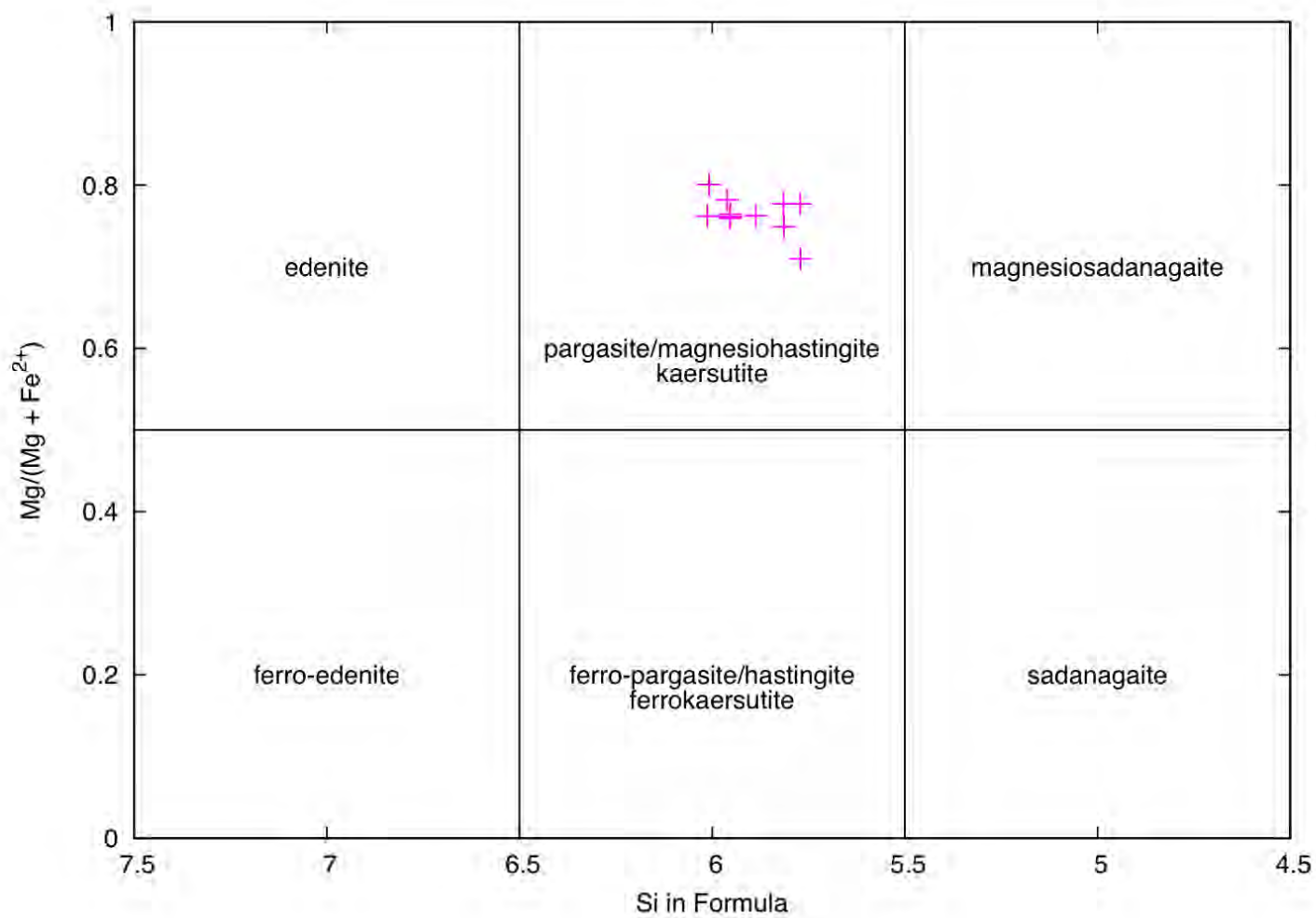


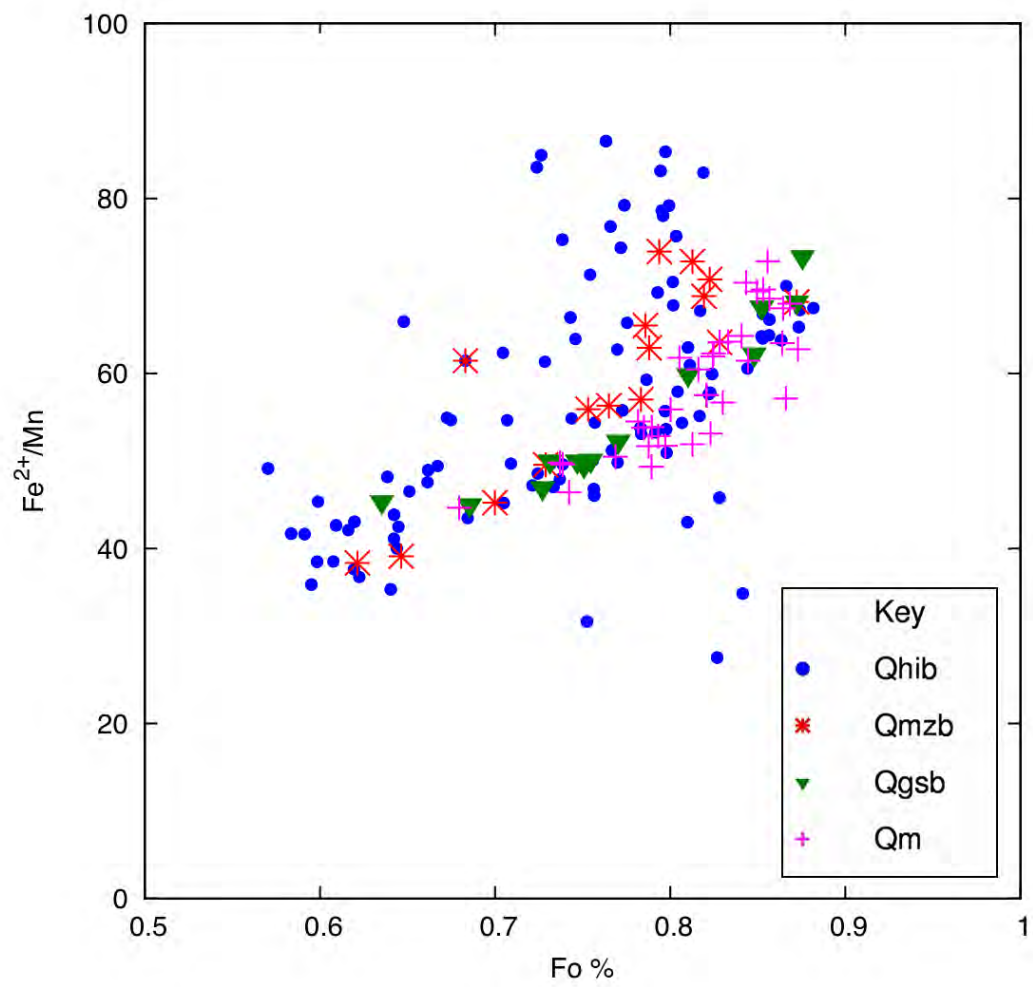


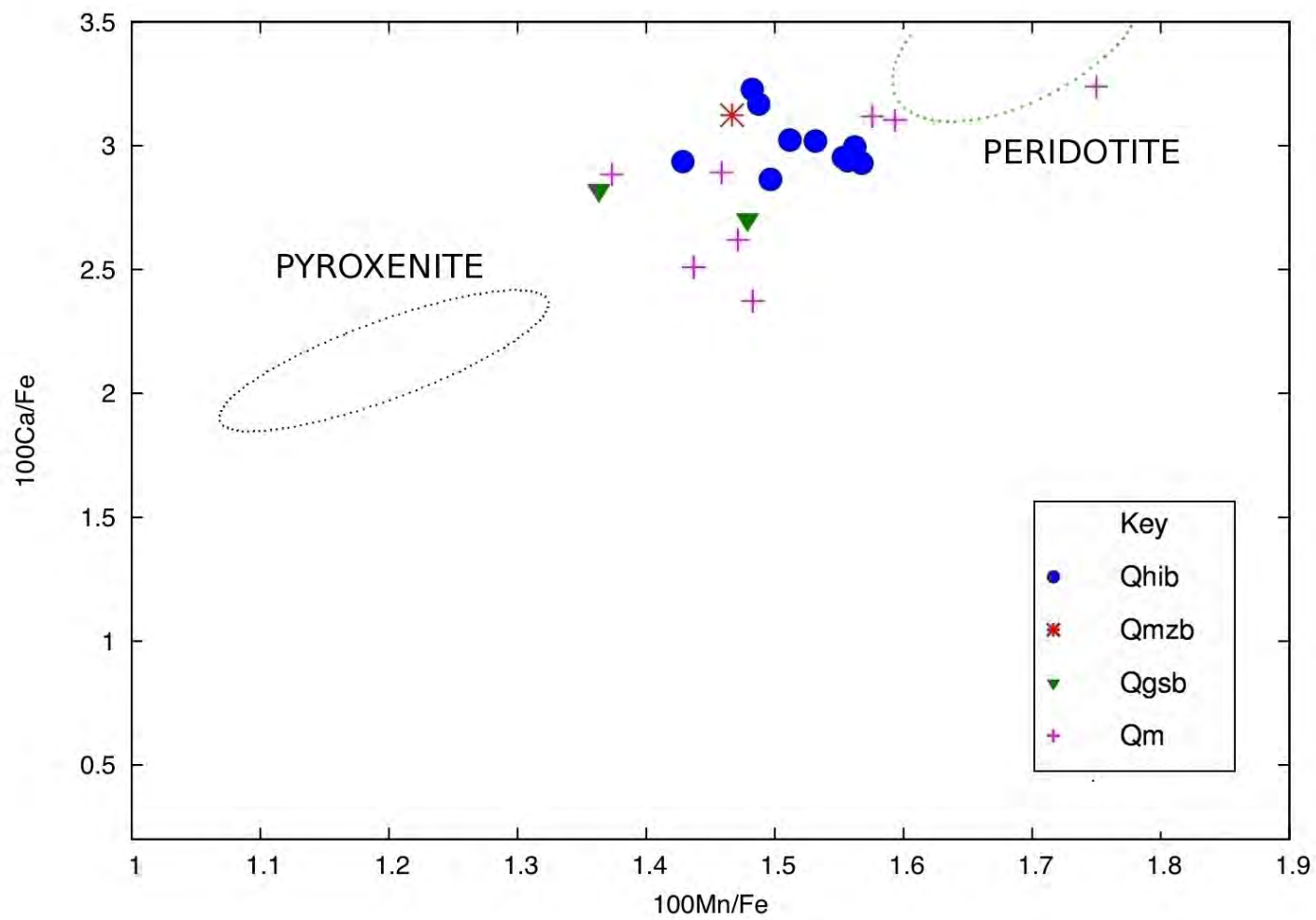




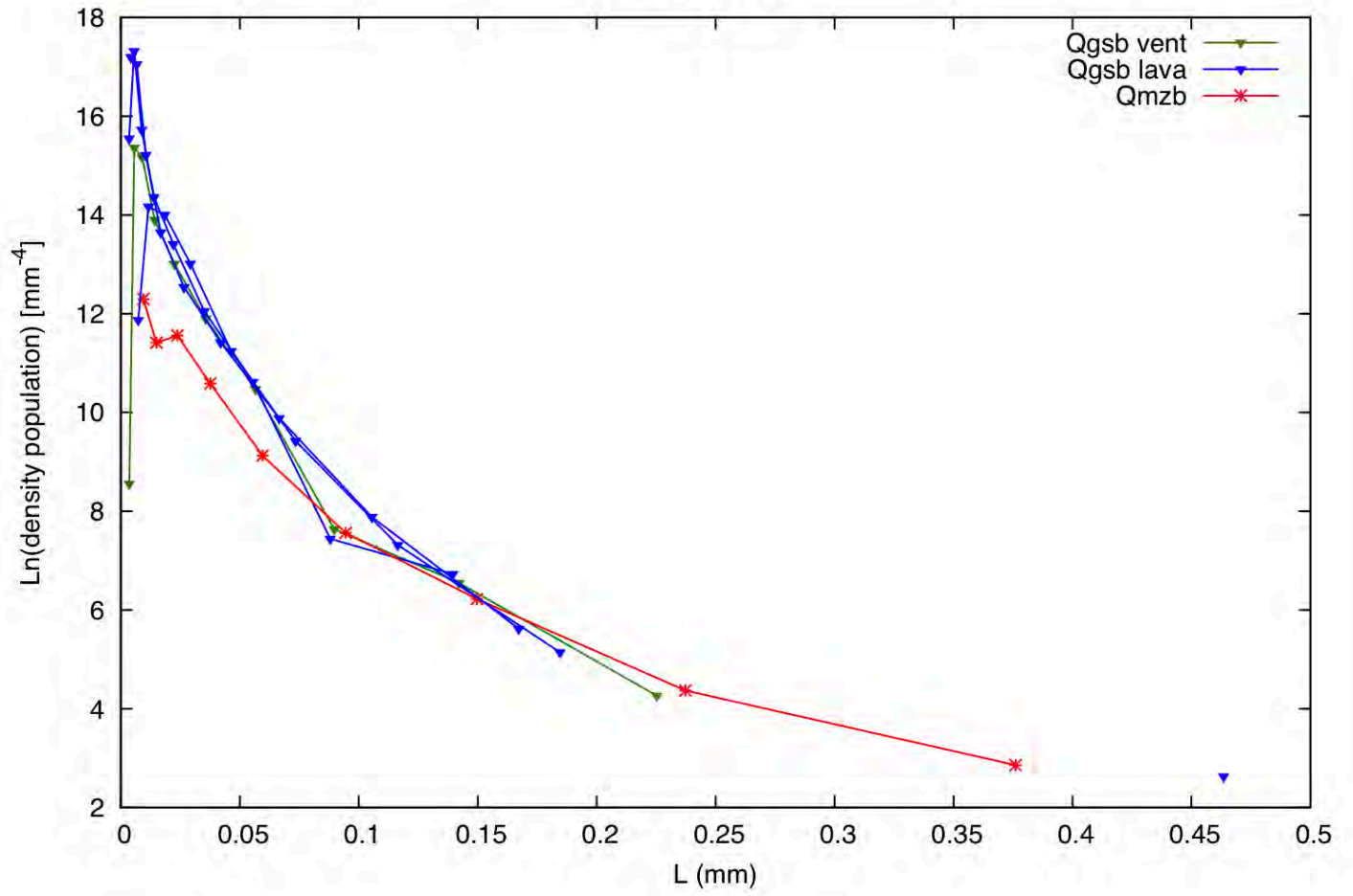




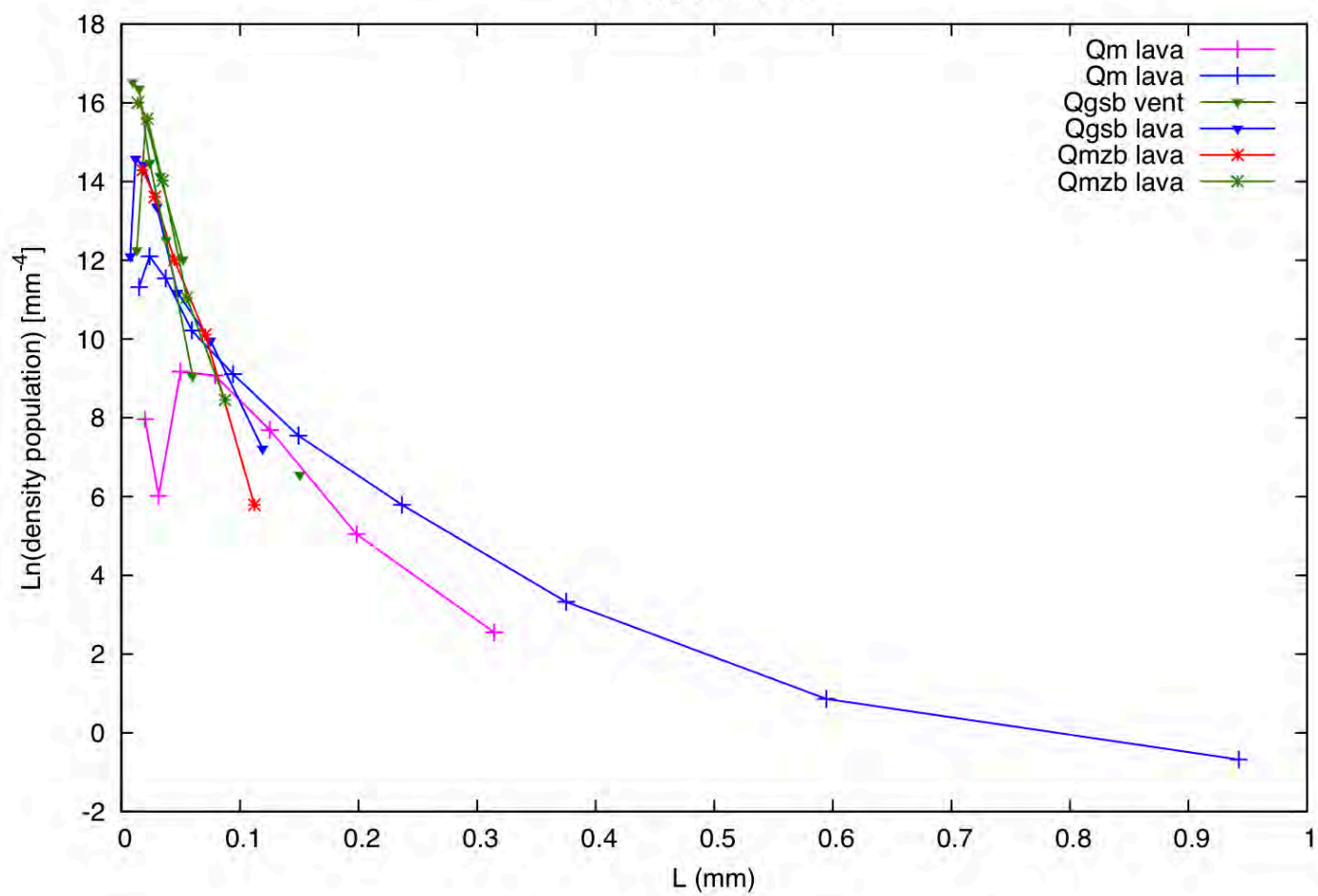




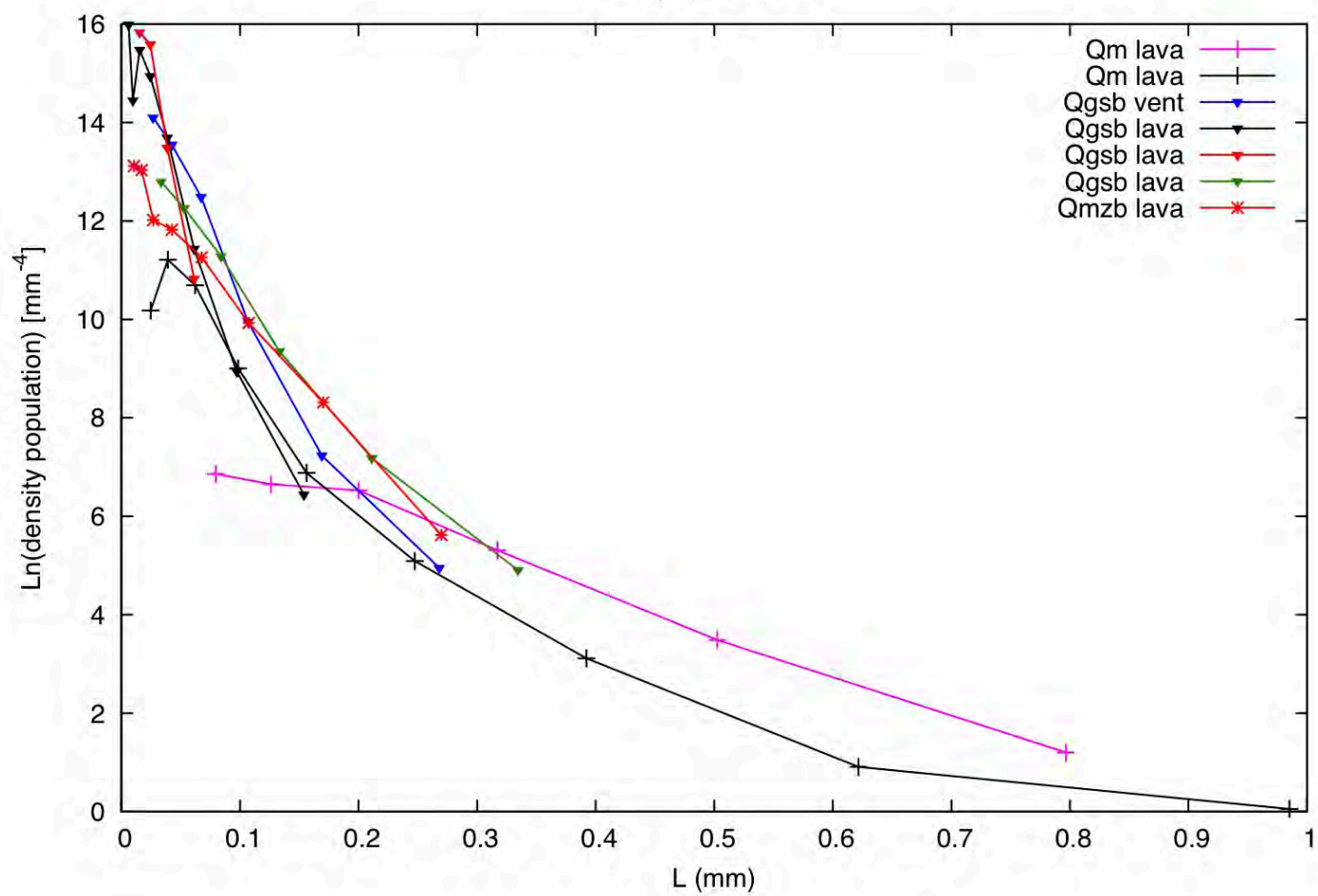
Olivine CSD



Clinopyroxene CSD



Plagioclase CSD





Oxides CSD

